Integrated Structural and Daylight Optimisation of Variable Transmittance Façades

Fady Abdelaziz[1,2], Samuel Esses[3], Kostas Grigoriadis[3*]

* Corresponding author: Corresponding author: k.grigoriadis@ucl.ac.uk
1 University College London, Bartlett School of Environment, Energy and Resources, Institute for Environmental Design and Engineering, United Kingdom
2 Cairo University, Faculty of Engineering, Department of Architecture, Egypt
3 University College London, Bartlett School of Architecture, Bartlett Faculty of the Built Environment, United Kingdom

Abstract

Traditional fabrication methods for plastic building panels, such as moulding and extrusion, have recently been advanced by large-scale robotic 3D printing (LSR3DP), enabling mass customisation and the production of complex architectural geometries. While existing research on LSR3DP has primarily focused on single-material printing, the exploration of multi-material or multi-property applications remains limited, especially at full architectural scale. This study addresses this gap by developing a performance-driven digital workflow for PETG-based façades that integrates structural efficiency with solar-responsive transmittance gradients. A multiobjective optimisation process using the Non-dominated Sorting Genetic Algorithm II (NSGA-II) generated 16 optimal façade geometries across four orientations (north, east, south, west), achieving up to 14% reduction in summer solar radiation and 26% increase in winter solar gain compared to a conventional vertical façade, while minimising structural displacement. The optimal south-facing solution was selected for detailed daylight performance assessment. A procedural gradient generation workflow was developed to discretise solar-based transmittance values across varying mesh densities and gradient resolutions. The best-performing variable transmittance configuration achieved 46.24% Useful Daylight Illuminance (UDI-a) and 69.21% spatial Daylight Autonomy (sDA), representing a 25.94% improvement in UDI-a over a conventional uniform-transmittance curtain wall. This integrated approach demonstrates LSR3DP's potential to produce unified, materially expressive façades that embed environmental performance directly into form and material logic, eliminating reliance on mechanical shading systems.

Keywords

Computational Design, Multi-property Façade Design, Multiobjective Optimisation, Daylight Performance

DOI

http://doi.org/10.47982/jfde.2024.350

1 INTRODUCTION

1.1 BACKGROUND

Plastics have been used in façade applications since 1954, initially in the form of glass-fibre-reinforced plastic (GRP) panels enclosing military radar domes (Engelsmann et al., 2010). A few years later, in 1957, the Monsanto House of the Future—designed by Monsanto, MIT, and WED Enterprises—was constructed using large GRP structural sections cantilevered from a concrete core, demonstrating the potential of this new material for building construction. Since then, plastics have been employed in a variety of applications (Engelsmann et al, 2010): *i)* as panels in building envelopes, such as the polycarbonate façade of the Laban Centre in London, UK, and the GRP façade of Terminal V in Lauterach, Austria; *ii)* as structural elements in sculptures, roofs, or pavilions, such as the Hoofddorp Bus Station (Castañeda et al., 2015) in the Netherlands; and *iii)* as both building structure and envelope, as seen in projects like FG 2000 in Altenstadt, Germany, which was constructed from composite GRP and PUR (Polyurethane) foam core structural sections.

In most of these examples, the plastic components were manufactured using injection moulding, casting, or extrusion—traditionally the primary fabrication methods for producing such parts or sections. Today, *Large-Scale Robotic 3D Printing (LSR3DP)* (Milano et al., 2024) has been added to these methods, offering capabilities that extend beyond mass production by enabling greater geometric complexity and adequate cost efficiency. One notable contemporary application of LSR3DP in architecture is the use of ABS (acrylonitrile-butadiene-styrene) plastic panels to clad the steel structure of the east gate at Nanjing Happy Valley Plaza in China (Yuan et al., 2022). The complex, non-repetitive geometry of the structure made a bespoke fabrication method such as LSR3DP particularly suitable, enabling the production of 4,000 unique panels in under two months. This technique is now being increasingly explored as a means of customising the geometry, performance, and finish of façade systems through the fabrication of bespoke, one-off panels.

Additionally, daylight control, typically achieved through mechanical shading devices, can instead be integrated directly using LSR3DP. This is because constructing such shading systems involves a complex assembly process. Another significant issue is "the cost of production and maintenance of sophisticated mechanical systems" (Vazquez & Duarte, 2022). Furthermore, these systems must be fixed to the building envelope using metal components, which introduces weak thermal points due to cold bridging. In contrast, the novelty of LSR3DP lies in its ability to minimise construction complexity, eliminate variability in thermal performance caused by the use of disparate materials and mechanical fixings, and avoid the ongoing maintenance typically associated with kinetic or conventional shading systems.

1.2 STATE OF THE ART

Research into the use of plastics in building façade panels has been ongoing for several years. This work can be divided into mono- and multi-material approaches: the former concerns the use of a single type of plastic across the entire panel, while the latter involves the fusion of plastics of different types, colours, or opacities. Within the mono-material category, sub-themes investigated include ventilation control and thermal heat storage (Mungenast, 2017); thermal performance (Sarakinioti et al., 2018; Piccioni et al., 2020); solar wall design and manufacturing (Tenpierik et al., 2018); and assessments of air permeability, water tightness, wind loads, and impact resistance

(Cheibas et al., 2024). Additionally, Milano et al. (2024) investigate the assembly of 3D printed plastic panels into a complete façade system, focusing on the interfaces between segments.

Of relevance to this study, Cheibas et al. (2023) examine various surface patterns on 3D-printed plastic panels to regulate daylight transmission and distribution, while Taseva et al. (2020) propose the use of circular gradient, truss gradient, and Schwarz P infill geometries in plastic panels for light control. In addition, the engineering practice Eckersley O'Callaghan and design studio Etcetera have undertaken research into "a building enclosure platform that replaces a typical multilayered façade build-up with a *unified* "single-material construction" (Quillet & Rogan, 2022), which is also directly relevant to this article.

Regarding the currently limited multi-material approaches, Grigoriadis (2018, 2019) presented research on design-to-fabrication workflows for a multi-material façade segment using PolyJet materials by Stratasys (Tee et al., 2020). Furthermore, Taseva et al. (2020) showcased a strategy for fabricating polyurethane foam-infilled, functionally graded plastic panels, and Kwon et al. (2019) presented an approach for combining carbon fibre-reinforced thermoplastics with polymers.

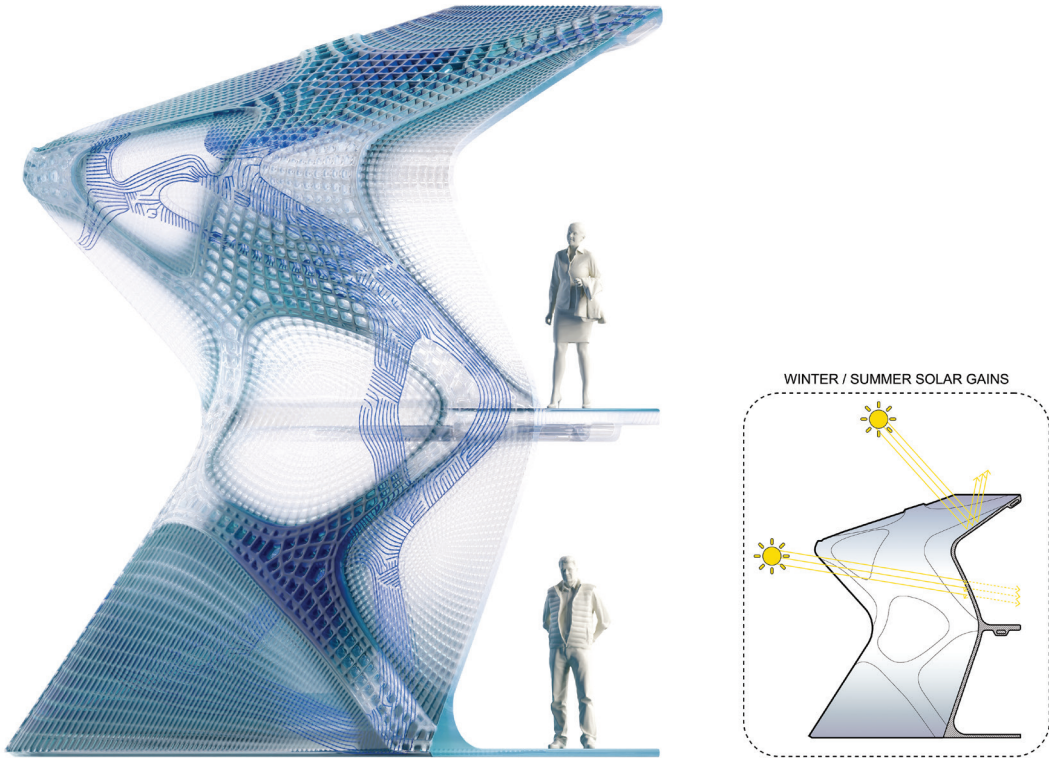

FIG. 1 Side view rendering of the MMIF project, illustrating the distribution of colour and transmittance gradients throughout the façade volume. This project served as the initial basis for the research presented in this paper.

1.3 CONTEXT

The study presented here builds upon the Multi-Material Integrated Façade (MMIF) project, shown in FIG 1 and FIG 2, initially developed by Grigoriadis and Esses and previously summarised in *3D Printing and Material Extrusion in Architecture: Construction and Design Manuals* (Grigoriadis & Lee,

2024). MMIF proposes a component-less building façade, designed and ultimately intended to be robotically fabricated, as a continuous volume characterised by gradual changes in transmittance and colour. In doing so, it effectively introduces a fourth category to those outlined in Section 1.1: the use of multi-properties or multi-materials in *iv*) a self-supporting envelope.

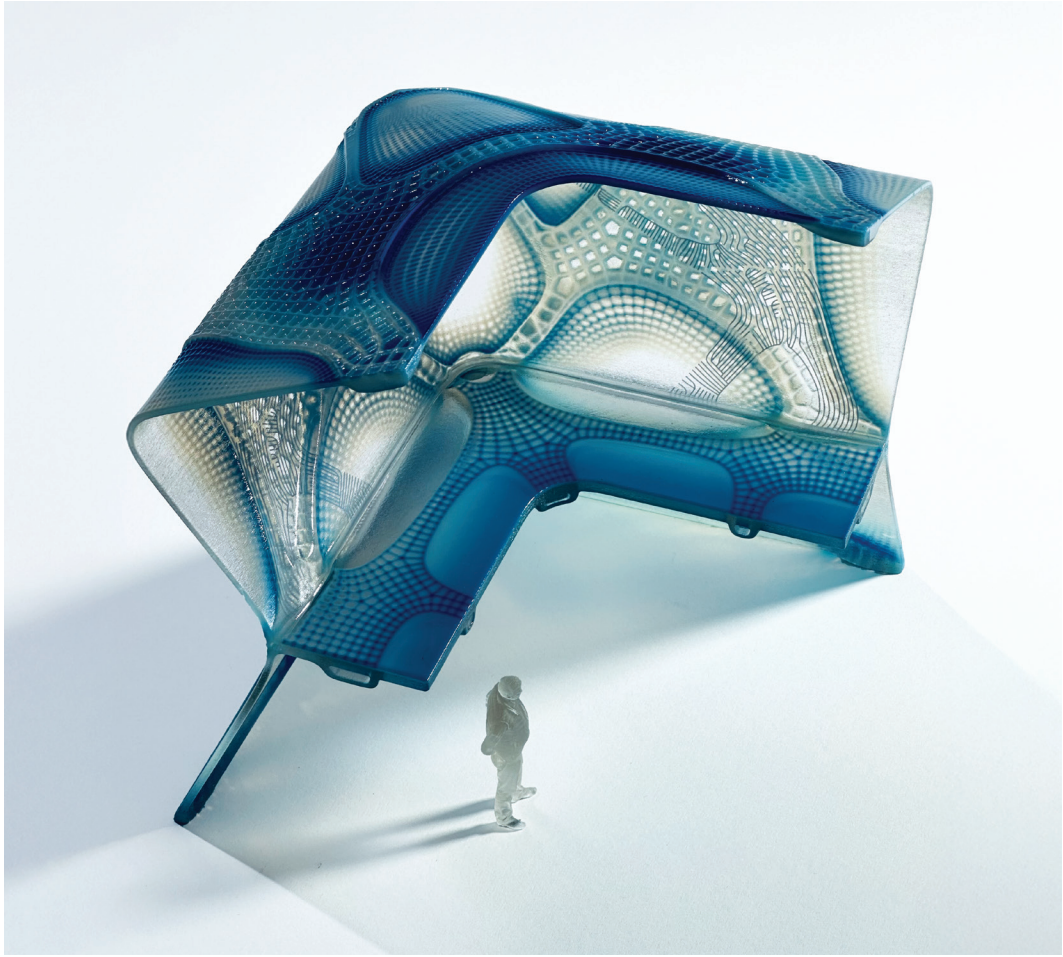

FIG. 2 View of the MMIF scale model printed with PolyJet materials on the Stratasys J835 multi-material 3D printer.

1.4 RESEARCH GAP

Current research on daylight control in 3D-printed façades has predominantly focused on geometric approaches, such as surface patterns, infill geometries, and layer orientation, rather than material-based transmittance gradients. Layered 3D printed geometry has been shown to create anisotropic optical behaviour through variations in layer height, width, and spatial configuration (Cheibas et al., 2023), whilst functionally graded façade elements using minimal surface infill structures have been developed, in which gradient effects emerge from wavelength and amplitude variations controlled by geometric parameters (Taseva et al., 2020). Similarly, research has demonstrated that 3D printing process parameters can tune optical properties from 90% transparency to 60% translucency (Piccioni et al., 2023). However, this tuning occurs through parameters that affect layer deposition rather than through variations in material composition across the façade surface. These studies consistently

control light transmission through physical form manipulation rather than through inherent variation in material optical properties.

This article advances this body of research by, for the first time, investigating the distribution and discretisation of continuous transmittance gradients across complex façade geometries to optimise performance. Whilst existing research achieves light control through geometrical articulation, the present work addresses how material properties can be systematically varied across a surface to achieve performance objectives. More specifically, it offers an alternative approach to previous studies (Cheibas et al., 2023; Taseva et al., 2020), focusing on the distribution of transmittance gradients rather than surface texturing or infill geometries. The study addresses two previously unexplored challenges: (1) specifying variable transmittance gradients across freeform geometries based on solar radiation data, and (2) developing discretisation strategies for translating continuous transmittance properties into stepped zones for daylight performance evaluation. This represents a significant gap, as no robust framework currently exists for the performance-driven application and discretisation of gradients, particularly for complex geometries enabled by LSR3DP.

The research that follows adopts a structured, multiobjective optimisation approach to balance summer and winter solar radiation with structural displacement criteria, determining an optimal façade form, illustrated in FIG 3. Multiobjective optimisation processes have typically been applied to the design of façade shading systems (Wagiri et al., 2024; Lin & Tsay, 2024; Fan et al., 2022), relevant to this study, to explore the relationship between glazing types, insulation, window-to-wall ratios, Useful Daylight Illuminance (UDI), and life cycle cost (Shan & Shi, 2016).

Building on this foundation, the optimisation process presented in this article consists of a bespoke workflow that distributes transmittance gradients across the continuous global surface. Daylight metrics analyses accompany this to evaluate the impact of these gradients on interior lighting conditions.

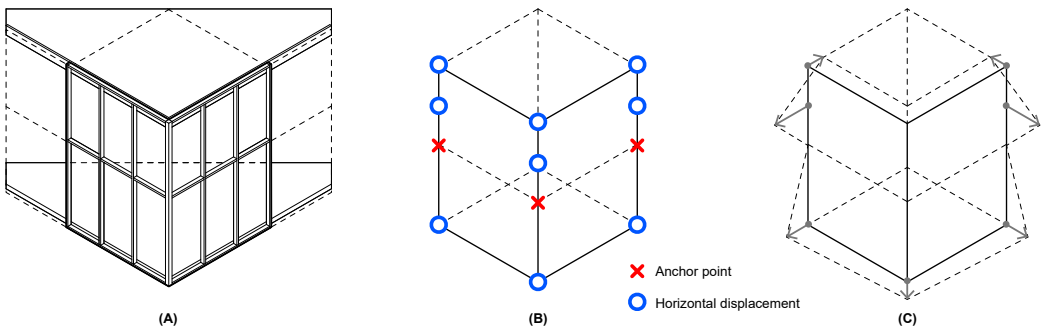

FIG. 3 Diagram of (a) the segment of the virtual building used as the baseline condition for the multiobjective optimisation, (b) the locations allowed to undergo displacement during optimisation, and (c) the geometry after displacement.

Effectively, this article addresses two key research questions:

1 How can multiobjective optimisation be applied to identify façade forms that balance summer solar radiation reduction, winter solar gain maximisation, and structural displacement minimisation?
2 How can solar-informed transmittance gradients be systematically distributed and discretised across façade geometries to achieve comfortable internal daylight levels?

2 METHODOLOGY

The methodological framework of this study comprises two distinct phases: form finding and gradient-based daylight performance analysis. This two-phase approach reflects the hierarchical nature of façade performance optimisation, in which geometric configuration must be established before material properties can be meaningfully assigned.

Phase 1 addresses the first research question by identifying optimal façade forms that balance competing environmental and structural criteria through multiobjective optimisation. This phase focuses on generating façade geometries through parametric modelling, evaluating their environmental and structural performance through coupled analysis, and identifying optimal configurations that balance competing criteria through evolutionary optimisation algorithms.

Phase 2 builds upon the optimised geometry to address the second research question by evaluating how solar-informed transmittance gradients influence interior daylight quality. This phase combines procedural modelling and discretisation techniques with a comprehensive evaluation of daylight performance based on validated simulation metrics.

This integrated approach, summarised in FIG 4, maintains continuity of geometric and performance data across both phases, ensuring that form-finding decisions directly inform the distribution of material properties.

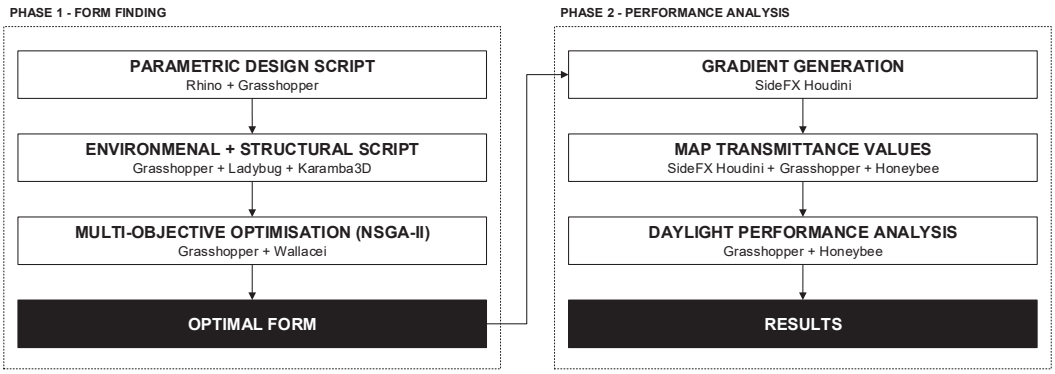

FIG. 4 Diagram summarising the methodology used in this study.

2.1 PHASE 1: FORM FINDING PROCESS

This phase establishes the methodological foundation for performance-driven façade design through parametric modelling, integrated environmental-structural analysis, and multiobjective optimisation. The process systematically explores how geometric variation influences solar exposure and structural behaviour, ultimately identifying configurations that achieve balanced performance across competing criteria.

2.1.1 Parametric Design Script

A parametric design approach was adopted to enable a systematic exploration of façade geometries with varying degrees of self-shading and structural articulation. Rhinoceros (Rhino) (Robert McNeel

& Associates, n.d.) and Grasshopper (Rutten and Robert McNeel & Associates, n.d.) were used to develop the parametric design script. These platforms were selected for their visual programming interfaces and seamless integration with environmental and structural analysis tools. Unlike fixed geometric configurations, parametric modelling allows the simultaneous investigation of multiple design variables and their combinatorial effects on performance, which is essential for identifying optimal solutions within a complex design space.

A corner façade geometry was selected as the case study, representative of typical commercial or office building construction. Eight primary parameters were utilised to articulate the façade with more control points than a typical vertical façade, enabling variations in profile depth, curvature, and corner orientation. These parameters were established to ensure geometric feasibility whilst maximising performance variation across environmental and structural criteria.

2.1.2 Environmental and Structural Analysis

The parametrically generated façade forms were assessed through an integrated environmental and structural analysis workflow within Grasshopper, using Ladybug (Roudsari and Ladybug Tools LLC, n.d.) for environmental analysis and Karamba3D (Preisinger, 2013) for structural analysis. Evaluating both aspects together was necessary, since geometric modifications that improve one criterion often compromise the other. The coupled approach supported the identification of configurations that achieve balanced performance across environmental and structural criteria.

Solar incident radiation was calculated for all façade iterations for summer and winter periods. The seasonal split was critical because effective façade performance requires low summer gains to reduce cooling loads and high winter gains to support passive heating. The analysis was conducted across four cardinal orientations (north, east, south, west), as solar exposure varies significantly with orientation and optimal geometric configurations differ accordingly. Ladybug was used for this analysis due to its validated solar-geometry algorithms and integration with Grasshopper, which enabled real-time feedback during parametric adjustments. The study used London Heathrow EPW data to provide hourly radiation values representative of the UK climate.

Structural displacement was calculated for all façade iterations to assess how each geometry responds to self-weight and applied loads. Displacement served as an indicator of structural efficiency and material use because larger values show higher structural demand that requires additional material or support to maintain stability, which influences fabrication feasibility and cost (Preisinger, 2013; Bollinger et al., 2010). Karamba3D was used for this assessment due to its finite element analysis capabilities and its integration within Grasshopper, which supported the combined environmental and structural workflow used to evaluate the parametrically generated façade forms.

PETG (Polyethylene Terephthalate Glycol) was specified as the façade material due to its demonstrated suitability for LSR3DP applications. PETG offers a favourable combination of durability, flexibility, and printability. It exhibits sufficient structural capacity for self-supporting façades whilst maintaining the flexibility necessary to accommodate thermal expansion and minor deformations without brittle failure (Piccioni et al., 2023a; Sarakinioti et al., 2018). Its optical properties also enable transmittance modulation, essential for Phase 2 of this research.

2.1.3 Multiobjective Optimisation and Pareto Solutions

A multiobjective optimisation process was conducted using Grasshopper and Wallacei (Showkatbakhsh et al., n.d.), employing the Non-dominated Sorting Genetic Algorithm II (NSGA-II) to identify façade geometries that balance competing environmental and structural performance criteria. This approach was necessary because the three performance criteria are inherently conflicting. Multiobjective optimisation enables exploration of the entire trade-off landscape, identifying solutions in which no objective can be improved without degrading at least one other objective (Deb et al., 2002).

Three objectives were selected to address fundamental façade performance requirements: (1) minimising summer solar radiation; reducing cooling demand and overheating discomfort; (2) maximising winter solar radiation; enhancing passive solar heating and reducing heating energy consumption; and (3) minimising structural displacement; ensuring material efficiency and fabrication feasibility, as excessive deformation would require additional material or structural reinforcement, compromising the viability of LSR3DP fabrication.

NSGA-II was employed through the Wallacei plugin for this optimisation process. NSGA-II was selected due to its established effectiveness in generating well-distributed Pareto-optimal solutions for multiobjective problems (Deb et al., 2002). The algorithm uses evolutionary operations such as selection, crossover, and mutation to refine a population of design solutions iteratively, maintaining diversity across the Pareto front while converging toward optimal performance. The optimisation was conducted independently for each cardinal orientation, as optimal façade configurations vary significantly with directional solar exposure.

The optimisation process generated Pareto fronts containing non-dominated solutions. To select a single representative solution from each Pareto front that balances all three objectives, the Technique for Order of Preference by Similarity to Ideal Solution (TOPSIS) was applied (Hwang & Yoon, 1981). TOPSIS is a multi-criteria decision-making method that ranks solutions based on their geometric distance from both an ideal solution (best possible values for all objectives) and a negative-ideal solution (worst possible values for all objectives). The solution with the highest preference score was selected as the TOPSIS-optimal solution for each orientation, providing a systematic approach for balancing competing objectives without arbitrary weighting schemes.

2.2 PHASE 2: DAYLIGHT PERFORMANCE ANALYSIS & TRANSMITTANCE GRADIENT GENERATION

Building upon the previous phase, this process utilises the Solar Incident Radiation data from Phase 1 and the Phase 1 Optimal Geometry (P1OG) as inputs. It follows a procedural workflow using SideFX Houdini (SideFX, n.d.) and further environmental simulations using Grasshopper and Honeybee (HB) (Roudsari and Ladybug Tools LLC, n.d.) to generate a gradient design and evaluate the daylight performance, aiming to establish a methodology for assessing daylight in additive-manufactured multi-property or multi-material façades. Houdini is used for its procedural modelling capabilities, which allow for rapid iteration and precise control over complex geometries and properties, such as colour and transmittance. Custom input/output (I/O) workflows were developed in Python to enable the structured transfer of data between the two platforms for environmental simulation, streamlining the computational process.

2.2.1 Gradient Generation

A procedural gradient-generation script was developed in SideFX Houdini using the P10G with the associated vertex colours from the solar radiation heatmap generated in phase 1. The P10G was simplified to three versions, low, medium, and high resolutions, by reducing the number of polygons used to represent the geometry. This was done to compare model complexity with analysis accuracy and runtime during the environmental simulations.

2.2.2 Gradient Discretisation

By discretising the gradient, the mesh was segmented into polygonal zones with shared colour values through attribute-based grouping. Promoting vertex colour attributes to the polygon level allowed polygons to be grouped into discrete model components for data transfer between SideFX Houdini and Grasshopper. This enabled an evaluation of how gradient resolution influences both the accuracy and computational performance of daylight metrics analyses, independent of mesh density. Higher numbers of discrete steps provide a closer approximation to the original continuous gradient. A custom VEX code was written in Houdini to convert the colour gradient into the desired number of discrete steps, summarised in FIG 5. This facilitated assigning stepped transmittance values across the geometry during the environmental simulations.

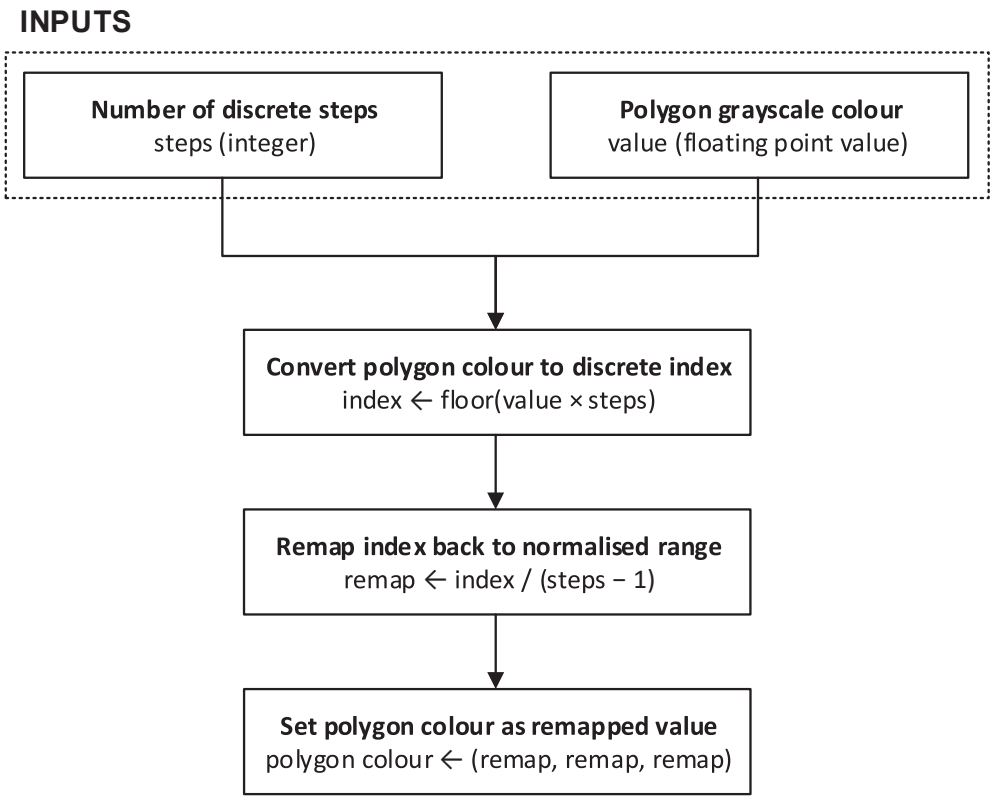

FIG. 5 Diagram of the method used for gradient discretisation.

2.2.3 Environmental Analysis

The output mesh groups were then evaluated within Grasshopper, using HB for environmental analysis. A custom Grasshopper component was developed in Python to construct a sorted list of model components based on their assigned colour values, enabling the mapping of grouped geometry to corresponding transmittance values in HB. Environmental inputs include weather data from the EPW file, the Daylight Autonomy (DA) threshold, and the occupancy schedule, which inform the analysis of DA and Useful Daylight Illuminance (UDI) experienced within the space. The analysis was conducted in two steps. (1) The first step aimed to evaluate the impact of mesh and gradient resolution on daylight analysis accuracy. (2) The second step aimed to identify the optimal range for the variable transmittance model to achieve both high daylight performance and visual comfort. Simulations were conducted on a laptop powered by an AMD Ryzen AI 9 365 processor, featuring 10 cores and 20 threads, with a base clock speed of 2.0 GHz and a maximum boost clock of 5.0 GHz.

3 RESULTS

This section presents the outcomes of the two-phase methodological process developed in this study. Phase 1 focuses on formulating input parameters, evaluating their sensitivity, and identifying optimal solutions based on multiple performance criteria. Phase 2 builds upon the selected geometry from Phase 1 to assess its daylighting performance and generate optimised transmittance gradient models.

3.1 PHASE 1: FORM FINDING PROCESS

This phase presents the form-finding process, summarised in FIG 6. Various form iterations are produced by manipulating the input variables, offering a range of design options for further analysis and optimisation. This consists of 3 key steps: (1) developing a parametric design script that systematically explores façade form options, (2) conducting a sensitivity analysis to test the impact of the building's geometry parameters on the environmental and structural performance, (3) developing a multiobjective framework for optimising the building form in response to the environmental and structural performance.

3.1.1 Parametric Design Script

The foundational geometry is a 6 × 6-meter rectangular footprint, extruded vertically to form a two-storey structure with a total height of 8 meters (4 meters per floor). This basic structure is consistently applied across all iterations, while the parametric flexibility focuses on designing and manipulating the corner wall façade.

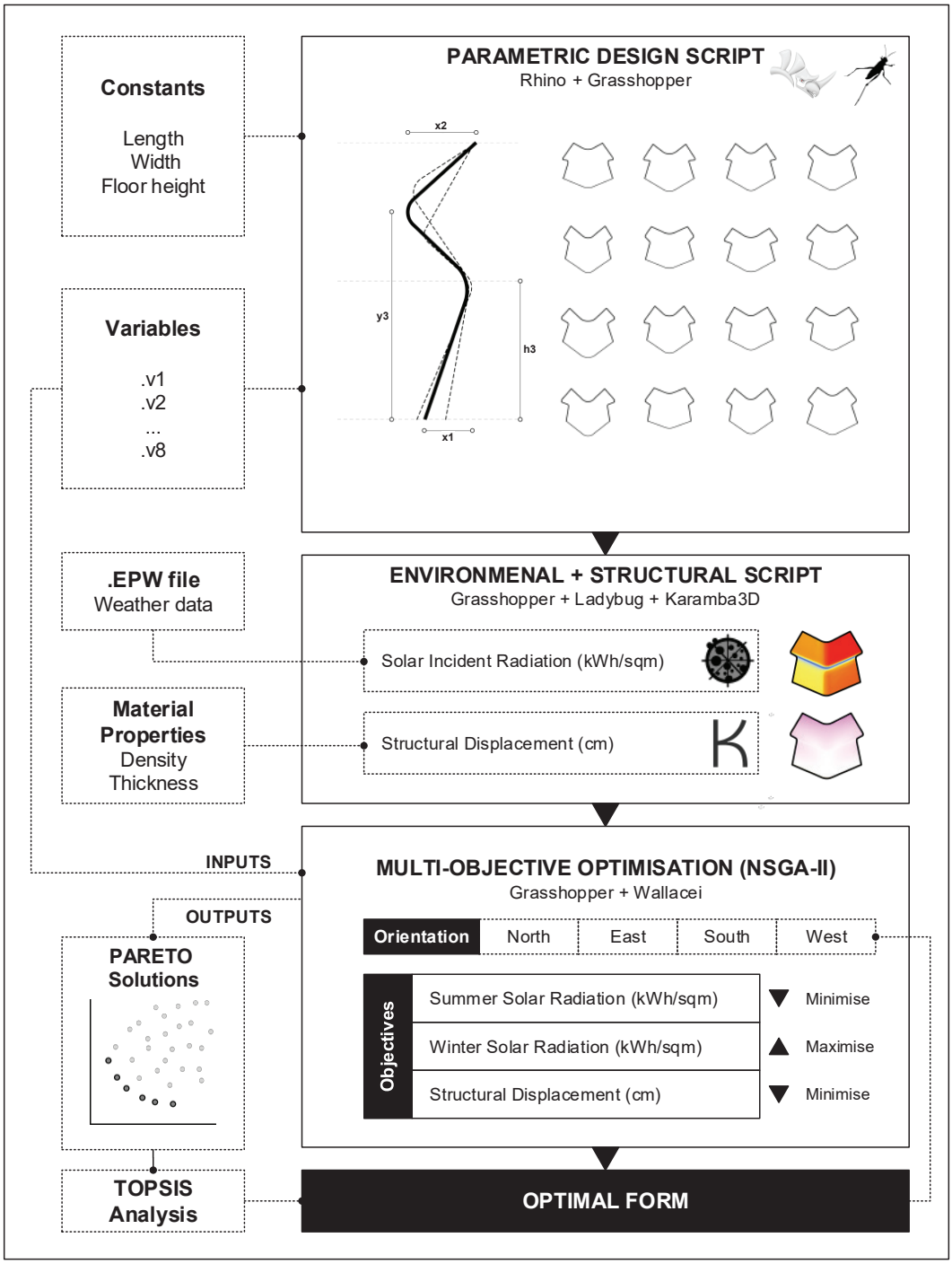

FIG. 6 Diagram summarising the workflow for Phase 1 of the study.

3.1.2 Key Parameters and Structure of the Façade Design

Eight primary parameters drive the generation of the corner wall façade, illustrated in FIG 7, each responsible for different aspects of its geometric configuration:

1. **Profile Articulation**: Six main parameters define the wall's corner profile, breaking the vertical line into three segments marked by four critical points:
    a. *Segment Division*: The vertical profile is segmented at specific points to delineate the ground and upper floors. The lower segment corresponds to the ground floor, while the upper segments represent the upper floor.
    b. *Point Displacements*: Four parameters control the positioning of points 1, 3, and 4 along the Y and Z axes. These points' displacements vary, allowing for a dynamic range of form iterations, each exhibiting unique variations in depth and shape across the façade. TABLE 1 outlines the range of values used for these displacements, enabling a structured yet flexible approach to façade modulation.
    c. *Curvature Control*: To add smoother transitions between segments, two more parameters were added to fillet the corners at points 2 and 3 on the vertical profile. The fillet radii at the points can be adjusted to create tight or loose façade curvature. The different curves of the wall create a sense of continuity along the façade, helping to smooth the transition between the ground and first-floor walls.

2. **Corner Profile Duplication and Orientation**: The main façade profile is duplicated and applied to both adjacent corners of the structure. Each profile copy is rotated by 45 degrees, orienting toward the square's centre, forming a cohesive wrap-around effect at each corner. The positioning of these corner profiles is adjustable through an additional parameter that allows each corner profile to shift either inward or outward relative to the square's corner, creating subtle variations in depth and spatial dynamics along the façade.

3. **Rail Profile Connectivity and Filleting**: Each of the four primary profiles is connected by a continuous rail element that unifies them vertically and horizontally, establishing a smooth transition across the façade segments. The final parameter controls the rail, which adjusts the fillet radius at the corners of the rail. Modifying the fillet creates rounded transitions between profiles, contributing to the façade's overall aesthetic.

4. **Lofting to Create the Façade Surface**: Once all profiles and rails are positioned, they are lofted together to form a continuous façade surface. This lofting operation integrates the profiles and rails into a single, cohesive surface, creating a dynamic façade structure that reflects the unique variations and adjustments defined by the parameters.

By fine-tuning these parameters, this workflow (FIG 8) generates a comprehensive array of façade iterations (FIG 9), each aligned with the core 6 × 6-meter building module, yet showcasing unique façade articulations for further analysis.

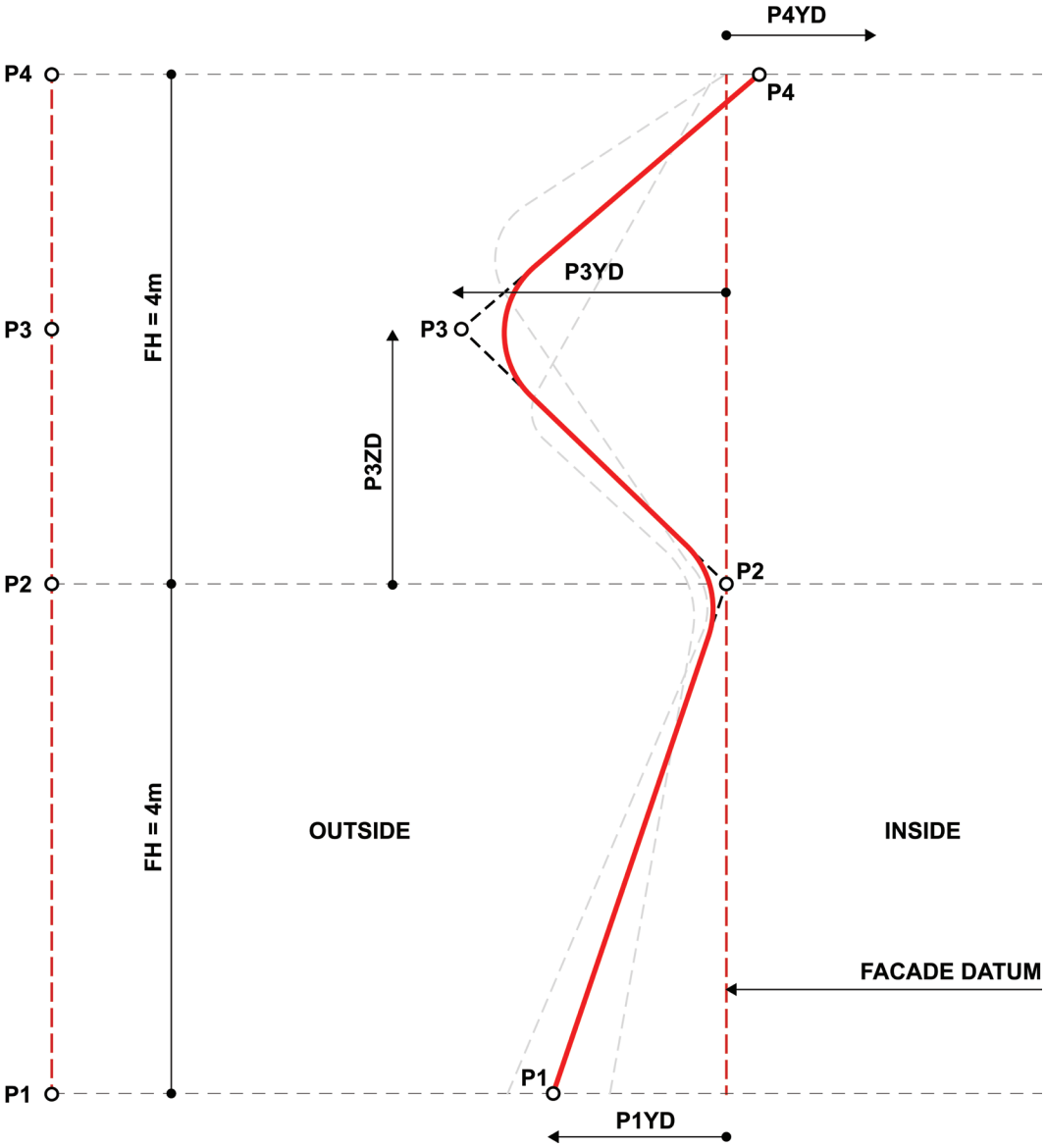

FIG. 7 Key parameters and structure of the façade design.

TABLE 1 Form-finding design parameters with value ranges used to iterate the model.

Parameter	Nomenclature	Value Range (m)	Type
Base-Square-Size	SS	6.0 * 6.0	Fixed
Floor-Height	FH	4.0	Fixed
Point-1_Y-Displacement	P1YD	0.5 - 2.0	Variable
Point-3_Y-Displacement	P3YD	1.5 - 3.0	Variable
Point-3_Z-Displacement	P3ZD	1.2 - 2.8	Variable
Point-4_Y-Displacement	P4YD	0.0 - 1.5	Variable
Point-2_Fillet-Radius	P2FR	0.25 - 1.0	Variable
Point-3_ Fillet-Radius	P3FR	0.25 - 0.5	Variable
Rail_Fillet-Radius	RFR	1.0 - 2.0	Variable
Corner_Displacement	CD	-1.5 - 1.5	Variable

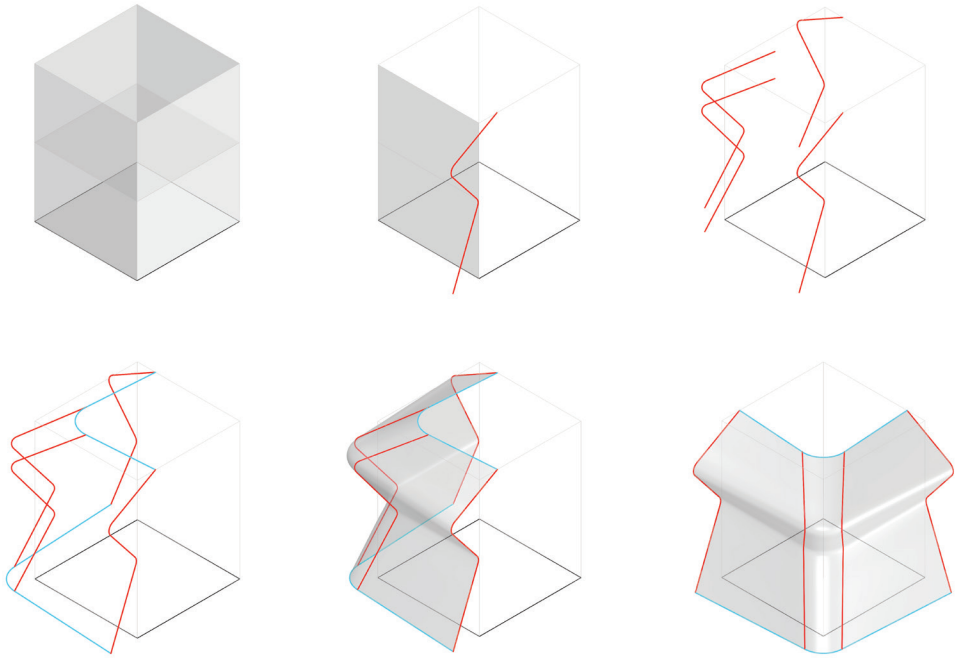

FIG. 8 Parametric generation sequence of the corner façade geometry, showing the transformation from a basic cubic volume to the articulated corner wall surface through the definition, manipulation, and lofting of vertical profiles (red lines).

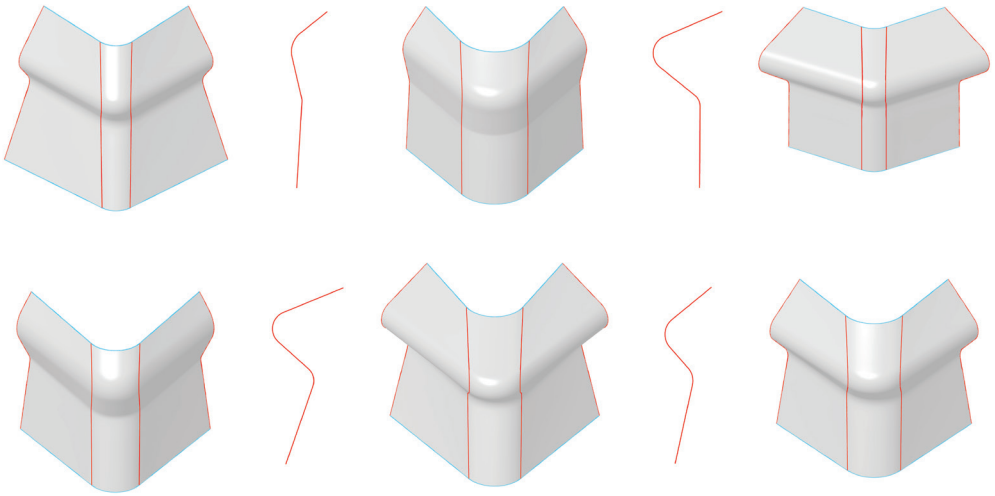

FIG. 9 Six design iterations generated from the parametric form-finding script. Each variation explores changes in key geometric variables that influence façade articulation and self-shading potential.

Environmental Performance

After generating the façade's lofted surface, the design script connects with an additional Ladybug script within Grasshopper to simulate annual solar radiation (FIG 10). This simulation uses the London Heathrow weather file as its climatic input. By applying this data to the façade, the script visualises the distribution of solar radiation across the surface over a typical year, highlighting areas of high and low solar exposure.

The analysis was conducted on the façade with four main orientations: north, east, south, and west. However, this study focuses primarily on the south orientation, which receives the highest solar radiation. To provide seasonal insights, the solar radiation was divided into two key periods: summer (March 21 to September 21) and winter (September 21 to March 21). The main objective is to reduce solar radiation during summer to minimise overheating and cooling energy demand, while maximising solar radiation in winter to enhance passive heating and energy efficiency. These insights are critical for developing optimised shading strategies and improving building performance.

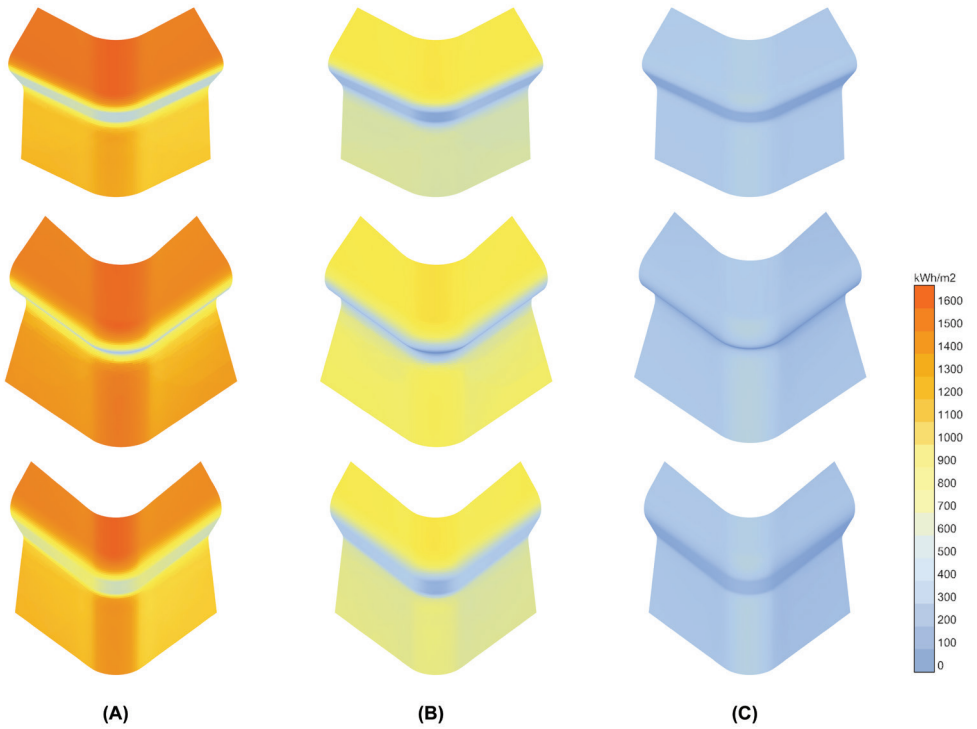

FIG. 10 Incident solar radiation visualisation for three different generated solutions. For each solution, the left column (A) shows the annual total solar radiation, the middle column (B) represents the summer season, and the right column (C) displays the winter season.

Structural Performance

In parallel, a Karamba3D script is integrated into the workflow to evaluate the structural displacement of the lofted surface, illustrated in FIG 11. Material properties are incorporated into the script, with an assumed façade thickness of 10 cm (TABLE 2). PETG's mechanical properties, including elasticity and density, are input into the script to estimate the surface's behaviour under various load conditions. This allows Karamba to calculate and visualise potential displacements or deformations, ensuring the façade's structural integrity.

The analysis assumed the façade structure is fixed only at the base, with gravity and material self-weight as the applied loads, illustrated in FIG 12. While in practice, the structure would be laterally supported by adjacent walls and connected to a roof structure above, analysing it as a self-structural envelope provides a conservative assessment of the façade's inherent load-bearing capacity. This approach isolates the performance of the façade geometry itself, independent of

auxiliary support systems, thereby evaluating whether the proposed unified envelope can maintain structural integrity under self-weight, a fundamental prerequisite before considering additional loading scenarios or integration with the broader building structure. This methodology also enables direct comparison across different geometric iterations without confounding variables introduced by varying support conditions.

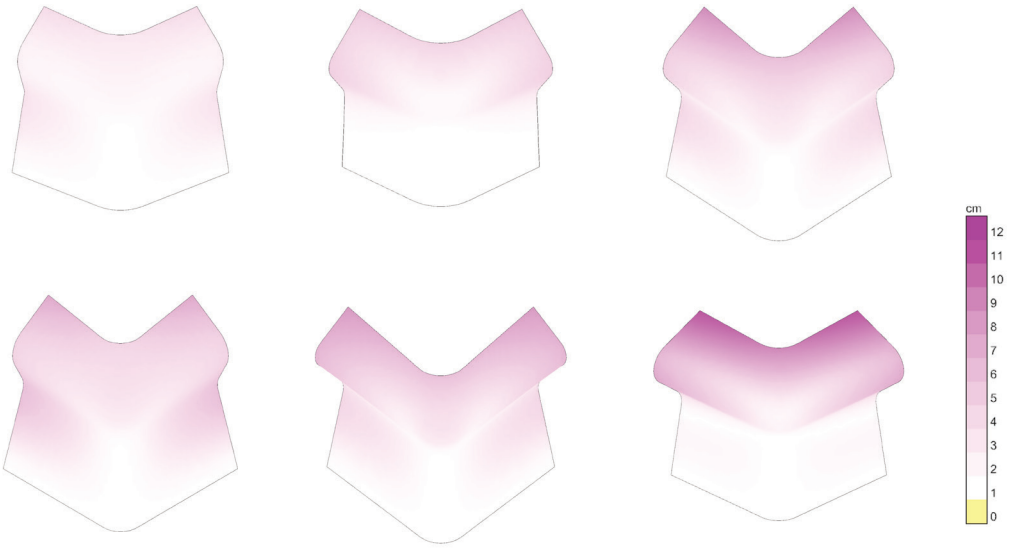

FIG. 11 Displacement of six façade iterations simulated in Karamba (Grasshopper) using PETG material properties. Darker colours indicate higher displacement, measured in centimetres.

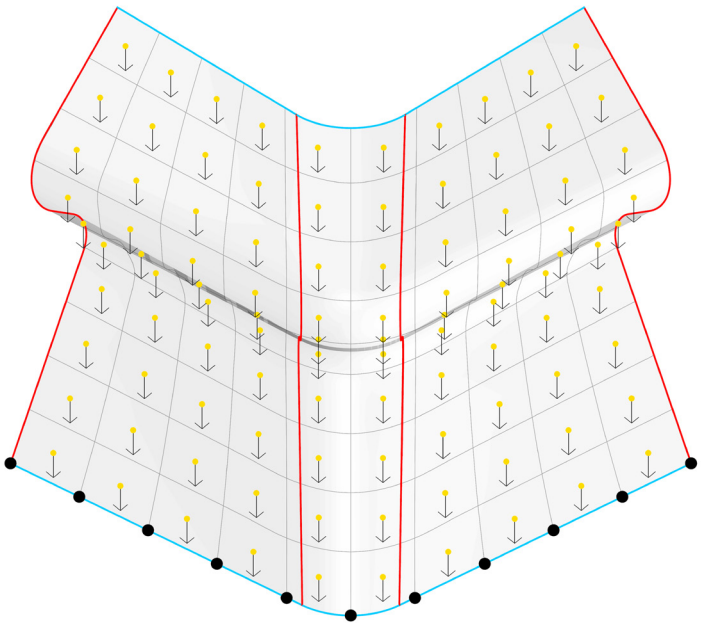

FIG. 12 Structural analysis model in Karamba showing the façade geometry with fixed boundary conditions at the base (black dots) and gravity loads applied to the structure (yellow dots with downward arrows). The red and blue edges delineate the façade profile boundaries.

TABLE 2 PETG material properties.

Material Property	Acronym	Value	Unit
Structure Thickness	T	10	cm
Young's Modulus	E	295	kN/cm^2
In-Plane Shear Modulus	G12	105.43	kN/cm^2
Transverse Shear Modulus	G3	105.43	kN/cm^2
Specific Weight	gamma	12.454	kN/m^3
Coefficient of Thermal Expansion	alphaT	0.000043	1/°C
Tensile Strength	ft	5.868	kN/cm^2
Compressive Strength	fc	5.868	kN/cm^2

3.1.3 Sensitivity Analysis for the Parameters

A sensitivity analysis was conducted to evaluate the relationship between the design parameters and three key objectives: summer and winter solar radiation, and displacement. A simple linear regression was performed for each parameter to assess its R-squared (R^2) value relative to these objectives, measuring the strength of the correlation and the proportion of variance explained. The method involved varying each parameter individually across its specified range, as outlined in TABLE 1, while keeping all other parameters fixed at their mean values. This approach enabled the isolated examination of each parameter's influence on the objectives. The analysis provided valuable insights into the varying degrees of impact and correlation that each parameter has with the design objectives, aiding understanding of their contributions, as outlined in TABLE 3.

Summer Solar Radiation

The analysis of summer solar radiation across various parameters reveals significant correlations with parameters P1YD, P3YD, P4YD, P2FR, P3DR, and RFR, with R-squared values ranging from 0.848 to 0.996. This indicates that these parameters account for a substantial proportion of the variance in solar radiation, suggesting that they are strong predictors. Parameter P3ZD shows a moderate correlation (R^2 = 0.781), whereas CD has the lowest R^2 (0.180), indicating the weakest correlation with summer solar radiation among the parameters. This suggests that CD accounts for only a minimal amount of the variance in summer solar radiation.

Winter Solar Radiation

The analysis of winter solar radiation across various parameters reveals significant correlations for most parameters, with R-squared values ranging from 0.814 to 0.992, indicating that they account for a substantial proportion of the variance in solar radiation and are strong predictors. Parameters P3ZD and P4YD exhibit notably lower R-squared values, 0.559 and 0.768, respectively, suggesting weaker explanatory power for variation in winter solar radiation than other parameters.

Displacement

The linear regression analysis shows strong correlations for parameters P1YD, P3YD, P3ZD, P4YD, P2FR, P3DR, and CD, with R-squared values ranging from 0.856 to 1.00. These parameters demonstrate a reliable linear relationship with the predicted façade displacements. In contrast, RFR exhibits the weakest correlation (R^2 = 0.603), reflecting a weaker linear association.

TABLE 3 Regression results for each parameter across the three objectives: Summer Solar Radiation, Winter Solar Radiation, and Displacement. Reported metrics include R-Squared, Mean Squared Error (MSE), Mean Absolute Error (MAE), Slope, and Intercept.

Objective	Parameter	R-Squared	MSE	MAE	Slope	Intercept
Summer Solar Radiation	P1YD	0.996	0.666	0.650	26.969	571.973
	P3YD	0.991	2.756	1.534	-37.105	689.594
	P3ZD	0.781	2.175	1.318	21.572	594.258
	P4YD	0.996	0.686	0.696	28.517	584.774
	P2FR	0.939	0.218	0.382	7.063	601.829
	P3FR	0.973	0.283	0.369	31.729	593.927
	RFR	0.848	1.057	0.868	-2.717	605.927
	CD	0.180	0.055	0.165	0.347	605.834
Winter Solar Radiation	P1YD	0.814	0.369	0.475	2.758	318.113
	P3YD	0.993	1.198	1.028	-27.471	383.555
	P3ZD	0.559	0.887	0.803	-8.215	325.123
	P4YD	0.768	0.340	0.456	-2.303	323.772
	P2FR	0.869	0.068	0.234	2.593	320.456
	P3DR	0.975	0.138	0.302	23.370	312.931
	RFR	0.992	2.278	1.185	-19.248	323.517
	CD	0.953	0.020	0.112	2.012	319.153
Displacement	P1YD	0.953	0.041	0.175	1.988	6.248
	P3YD	0.989	0.112	0.289	6.772	-6.366
	P3ZD	0.921	0.001	0.020	-0.609	8.826
	P4YD	0.990	0.064	0.216	5.559	4.602
	P2FR	0.856	0.000	0.005	-0.056	8.525
	P3FR	1.000	0.000	0.002	-3.334	9.749
	RFR	0.603	0.084	0.244	0.398	8.197
	CD	0.988	0.001	0.020	-0.699	9.520

3.1.4 Development of a Multiobjective Optimisation Framework

A multiobjective optimisation framework was developed to address the conflicting design goals. The framework utilised the Wallacei plugin within Grasshopper, which implements the NSGA-II to optimise multiple objectives simultaneously. This process was structured as described in the following paragraphs.

Parameter and Objective Definition

The process began by defining the design parameters and objectives. As detailed in TABLE 4, the parameters were carefully selected based on their influence on the design objectives, as determined by the sensitivity analysis. Eight parameters were defined, each representing a critical design variable. The possible values for each parameter were determined in 1 cm increments, resulting in a finely granular range of options.

This granular approach resulted in a vast search space of possible design solutions, calculated as the product of the possible values for all eight parameters. The total number of potential solutions was approximately 8.5 quadrillion. Such an extensive search space highlights the complexity and computational challenge of the optimisation process, as it was impractical to evaluate all possible combinations exhaustively. This further emphasised the need to employ advanced optimisation algorithms, such as NSGA-II, to explore the search space and efficiently identify optimal solutions.

TABLE 4 Design Parameters, Value Ranges, and Search Space for Form Generation.

Parameter	Parameter	Value Range (m)	Number of Values
Base-Square-Size	SS	0.5 – 2.0	151
Floor-Height	FH	1.5 – 3.0	151
Point-1_Y-Displacement	P1YD	1.2 – 2.8	41
Point-3_Y-Displacement	P3YD	0.0 – 1.5	151
Point-3_Z-Displacement	P3ZD	0.25 – 1.0	76
Point-4_Y-Displacement	P4YD	0.25 – 0.5	26
Point-2_Fillet-Radius	P2FR	1.0 – 2.0	301
Point-3_ Fillet-Radius	P3FR	-1.5 – 1.5	101
Rail_Fillet-Radius	RFR	1.0 - 2.0	Variable
Corner_Displacement	CD	-1.5 - 1.5	Variable
	Number of possible solutions [Search Space] 8,479,876,127,884,620		

The sensitivity analysis revealed a critical relationship between the objectives: summer solar radiation and displacement were directly proportional, while winter solar radiation was inversely proportional to both. This interplay introduced additional complexity to the optimisation process, as improving one objective often adversely affected another.

Optimisation Process

The framework was configured with 50 generations and 20 genes per generation, resulting in 1,000 runs. Each design solution, represented as a gene, was evaluated against the three objectives, with the algorithm iteratively refining the solutions through genetic operations, including crossover, mutation, and selection. The result was a Pareto front of non-dominated solutions, where no objective could be improved without worsening at least one other objective. These solutions represented the trade-offs between the conflicting objectives, providing a comprehensive view of the optimisation landscape. To ensure robustness and prevent premature convergence to a local optimum, the optimisation was run multiple times with different initial combinations of design variables. This approach helped explore the search space more thoroughly and increased the likelihood of identifying global optimum solutions.

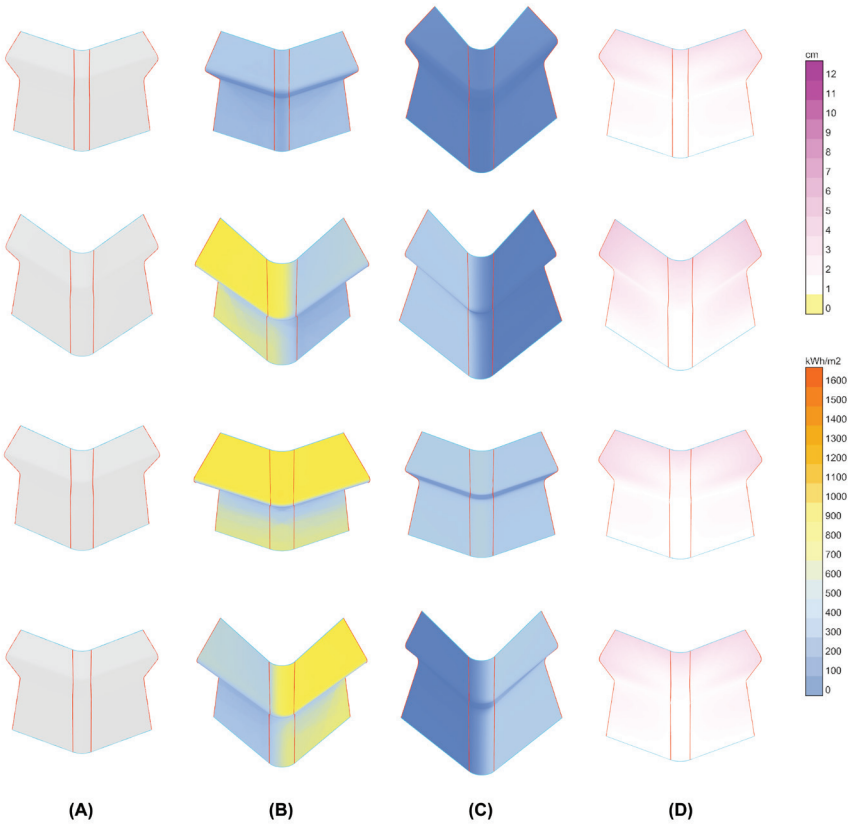

FIG. 13 Visual comparison of the 16 optimal façade solutions categorised by optimisation objective and orientation. Column (a) presents the solutions selected using the TOPSIS method, while columns (b), (c), and (d) show the solutions optimised individually for summer solar radiation, winter solar radiation, and displacement, respectively. Each row corresponds to a specific orientation, from top to bottom: north, east, south, and west, respectively. The colour maps represent solar radiation in kWh/m^2 and displacement in cm.

Optimisation Results

A total of 16 optimal façade solutions were identified through the multiobjective optimisation process, with four optimal configurations generated for each orientation (north, east, south, and west), illustrated in FIG 13. These included the TOPSIS-based optimal solution, along with optimised solutions for summer solar and winter solar radiation, and structural displacement. The results show variation across objectives, with some trade-offs observed between solar performance and displacement. Notably, for both the north and west façades, the displacement-optimal solution coincided with the TOPSIS-optimal one, indicating that in these cases, minimal deformation was aligned with a balanced solar performance. This overlap suggests that specific design configurations can simultaneously meet both structural and environmental criteria, thereby reducing the need for further compromise or adjustment.

The analysis of the optimisation results reveals several key insights into the relationship between solar performance, structural displacement, and surface area. South-facing façades consistently exhibited the highest levels of both summer and winter solar radiation, confirming their critical role in passive solar design. However, these orientations also showed moderate displacement values, indicating a potential trade-off between solar gain and structural flexibility. In contrast, the north façade received the lowest solar radiation but achieved the smallest displacements, making it more

structurally stable but less effective for energy capture. The east and west façades demonstrated greater variation in both displacement and solar values, highlighting their performance sensitivity to specific geometric configurations. The surface area was generally larger in solutions optimised for solar gain, suggesting that increased exposure often came at the cost of higher deformation. These findings underscore the importance of orientation-specific design strategies and the value of multiobjective optimisation in achieving balanced façade performance.

To evaluate the performance gains, all solutions were benchmarked against a traditional vertical façade with an identical footprint (6 m x 8 m per façade). The improvement analysis reveals that the optimal summer solar solutions achieved reductions in summer solar radiation ranging from 7.30% (west) to 13.99% (north) compared to the conventional vertical configuration. Simultaneously, the optimal winter solar solutions demonstrated substantial increases in winter solar gain, ranging from 3.61% (west) to 26.80% (north), highlighting the capacity of geometrically articulated façades to enhance passive solar heating during colder months (TABLE 5).

TABLE 5 Comparison of façade solutions based on TOPSIS ranking, summer and winter solar radiation performance, displacement, and surface area across four orientations. The table presents the optimal solution according to the TOPSIS method alongside solutions optimised individually for summer solar gain, winter solar gain, and structural displacement.

	Objective	Traditional Façade	TOPSIS Optimal Solution	Optimal Summer Solar Solution	Optimal Winter Solar Solution	Optimal Displace-ment Solution	Improve-ment	Unit
North	Summer Solar	355	319.33	305.33	466.84	325.74	13.99%	kWh/m²
	Winter Solar	96	87.40	85.19	121.73	88.01	26.80%	
	Displacement	-	1.71	2.50	7.59	1.66	-	cm
	Surface Area	96	93.86	94.31	153.45	95.29	-	m²
East	Summer Solar	460	466.61	423.31	500.42	466.61	7.98%	kWh/m²
	Winter Solar	212	210.17	192.88	226.01	210.17	6.61%	
	Displacement	-	2.56	8.49	6.60	2.56	-	cm
	Surface Area	96	120.10	154.76	149.36	120.10	-	m²
South	Summer Solar	591	581.38	530.58	616.74	594.22	10.22%	kWh/m²
	Winter Solar	346	353.57	327.78	379.45	374.74	9.67%	
	Displacement	-	2.33	9.54	2.56	1.78	-	cm
	Surface Area	96	102.41	115.33	97.37	95.46	-	m²
West	Summer Solar	486	517.80	450.54	504.45	517.80	7.30%	kWh/m²
	Winter Solar	230	211.80	212.38	238.31	211.80	3.61%	
	Displacement	-	1.81	7.19	4.37	1.81	-	cm
	Surface Area	96	97.12	152.13	146.00	97.12	-	m²

These quantitative improvements demonstrate the efficacy of the multiobjective optimisation framework in generating façades that outperform conventional planar configurations across multiple environmental criteria.

Analysis of the South-Oriented Façade Pareto Front

To build on the broader optimisation findings, this section provides a deeper analysis of the south-oriented façade, examining how the three objectives interact across its Pareto front. The south orientation was selected for detailed analysis because of its critical role in passive solar design. Among all façades, it consistently received the highest levels of solar exposure, making

it especially relevant for evaluating both thermal and daylighting performance. Focusing on this orientation enables a clearer understanding of the trade-offs between solar control and structural behaviour. It provides a well-suited basis for selecting a geometry to carry forward into the daylight simulation phase.

The Pareto front analysis of the south-facing façade reveals a clear trade-off landscape between the three primary performance objectives: minimising summer solar gain, maximising winter solar access, and reducing structural displacement. As shown in FIG 14, the 3D scatter and corresponding 2D plots illustrate a well-defined Pareto frontier, where solutions begin to cluster along a curved edge, indicating non-dominated performance trade-offs. Summer and winter solar gains exhibit a positive correlation, while both are inversely related to displacement. This suggests that improving environmental performance often comes at the cost of increased deformation, particularly when surface area is expanded to capture more solar radiation.

TABLE 6 Design parameter values for the four selected south-facing façade solutions: the TOPSIS Optimal Solution, the Optimal Summer Solar Solution, the Optimal Winter Solar Solution, and the Optimal Displacement Solution.

Parameters	TOPSIS Optimal Solution	Optimal Summer Solar Solution	Optimal Winter Solar Solution	Optimal Displacement Solution	Unit
P1YD	0.52	0.51	1.15	0.75	m
P3YD	1.67	2.83	1.53	1.55	
P3ZD	0.59	0.30	0.40	0.60	
P4YD	0.04	0.02	0.20	0.05	
P2FR	0.62	0.35	0.75	0.57	
P3FR	0.35	0.34	0.35	0.33	
RFR	1.28	1.65	1.54	1.34	
CD	-0.78	-1.38	-1.46	-1.39	

From this analysis, four key solutions were extracted and compared in TABLE 6: the TOPSIS-optimal solution, the solutions optimised individually for summer solar gain, winter solar gain, and displacement. These options span the Pareto front, capturing different prioritisation strategies within the solution space. The TOPSIS solution offers a balanced compromise between the three objectives, with moderate solar values and relatively low displacement. In contrast, the summer solar-optimal solution significantly reduces exposure, albeit at a higher displacement and with a larger surface area to provide shade on the lower part of the façade. The winter solar-optimal solution captures the most solar gain in colder months but is also associated with increased surface area and corresponding structural impact. The displacement-optimised solution achieves the lowest deformation while still maintaining moderate solar performance.

This comparative analysis is essential in selecting the candidate for further daylight investigation in Phase 2. The TOPSIS-optimal geometry was ultimately chosen for its well-rounded performance across all objectives. Unlike extremes that prioritise one criterion at the expense of others, this solution offers a balanced design that integrates solar exposure control with structural efficiency. Furthermore, its moderate form of complexity made it suitable for applying transmittance gradients without introducing excessive simulation burden. This decision ensured continuity between performance-based form finding and the subsequent daylight optimisation process.

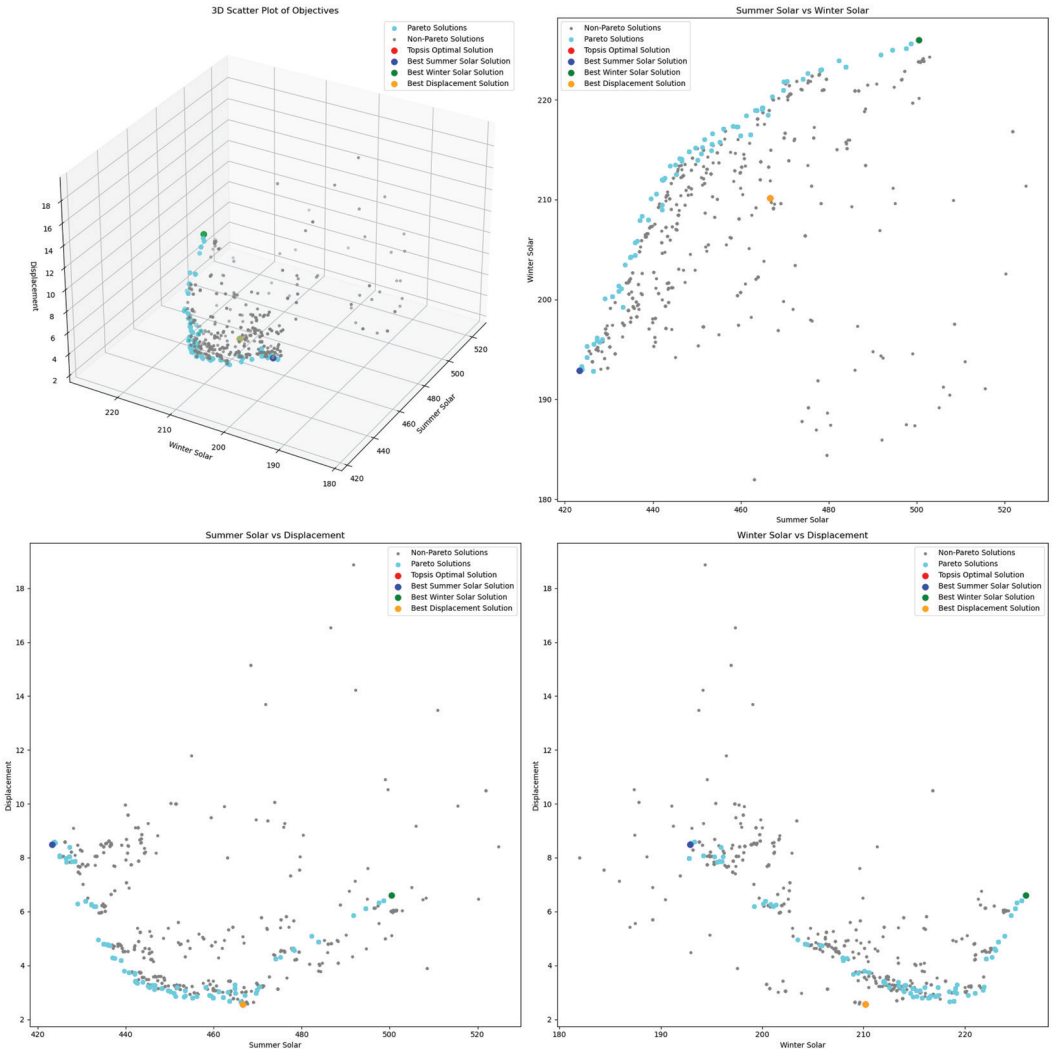

FIG. 14 Optimisation Pareto Front for the south-oriented façade.

3.2 PHASE 2: DAYLIGHT PERFORMANCE ANALYSIS & TRANSMITTANCE GRADIENT GENERATION

The primary objective of this phase was to conduct a daylight performance analysis of the transmittance gradient design, utilising the P10G, to determine the optimal transmittance values for achieving indoor daylight levels and daylight comfort. This phase consists of two key steps: (1) generating optimised variable transmittance models and (2) conducting daylight performance analysis of the optimised models, summarised in FIG 15.

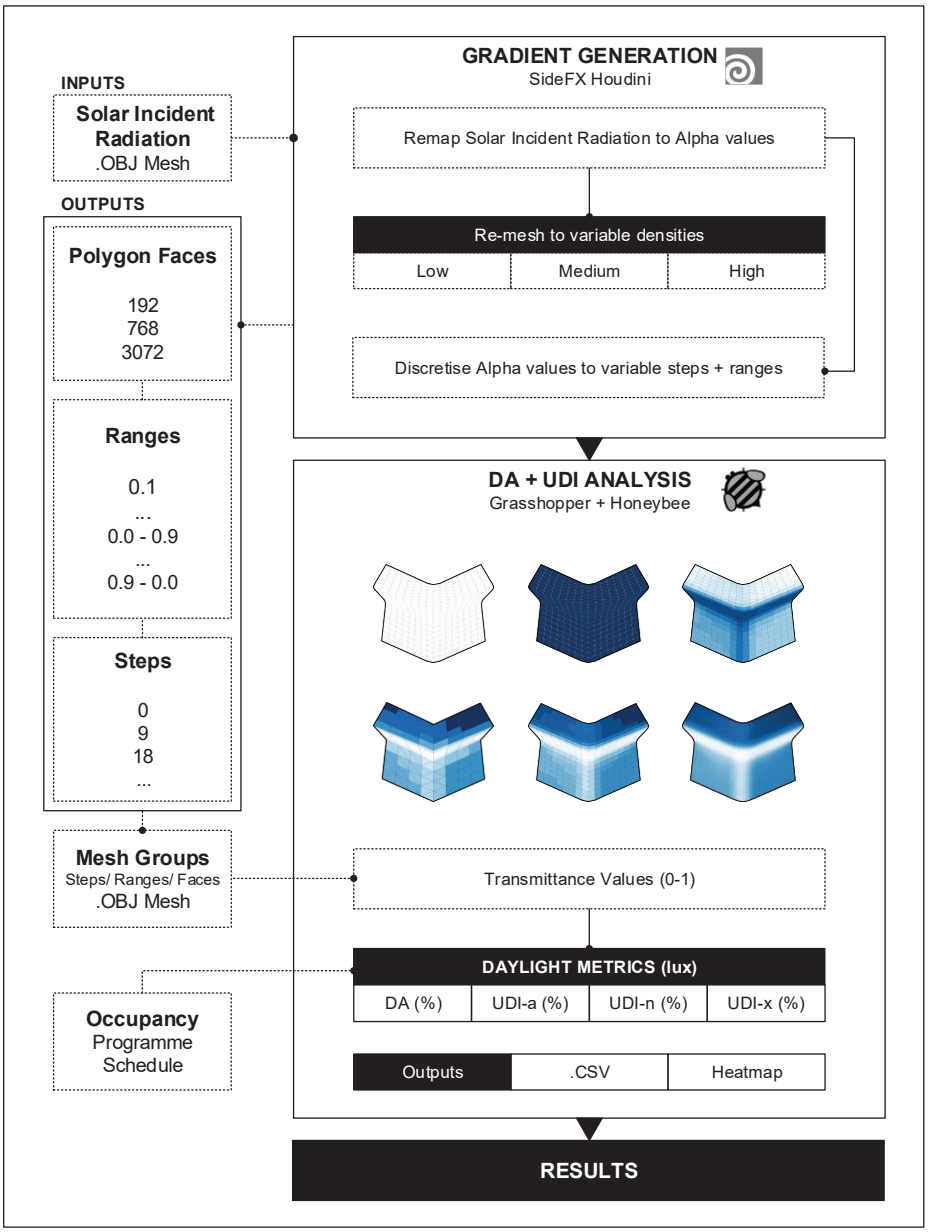

FIG. 15 Diagram summarising the workflow for Phase 2 of the study.

3.2.1 Optimised Gradient Transmittance Models

Various models were generated by reconstructing the P10G at different mesh densities and discretising the gradient into a series of varying step resolutions. It was essential to optimise the model to avoid unnecessarily long simulation times during the daylight performance analysis. This provided an opportunity to compare model complexity, defined by mesh and gradient resolution, against analysis accuracy and simulation runtime to identify the point at which increased model resolution no longer yielded significant benefits. P10G, containing the whole year radiation heatmap, was used in the following steps.

Gradient Generation

The heatmap was converted into a linear grayscale gradient and normalised to the range 0 to 1. Alpha (transparency) values were then assigned to each vertex directly from these remapped values. To enhance the visual distinction of the opaque-to-transparent gradient, a colour was applied to the model gradient. This resulted in a continuous façade geometry exhibiting variable optical properties in both colour and opacity, as illustrated in FIG 16.

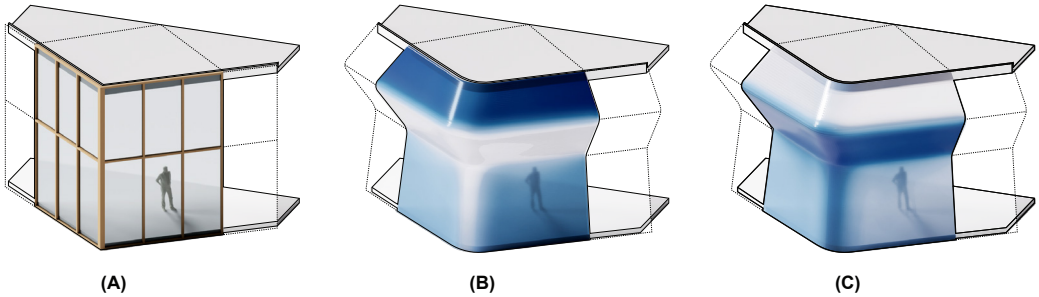

FIG. 16 Diagrams of (a) the standard curtain wall façade, (b) the gradient design on the optimal geometry (blue represents opacity; and white, transparency), (c) the inverted gradient design on the optimal geometry (blue represents opacity; and white, transparency).

Optimised Model Variations

The geometry was reconstructed into a simplified mesh, preserving the displacement parameters of the model profile from the optimal solution, and subdivided into three density versions, Low Poly (LP), Medium Poly (MP), and High Poly (HP), as shown in TABLE 7. An *Attribute Transfer* operation in SideFX Houdini was used to map the solar radiation heatmap, stored as vertex colours, of the original mesh onto the simplified mesh. This function transfers attributes based on spatial proximity (SideFX, n.d.). The colour gradient was discretised into a varying number of steps for each simplified mesh, shown in FIG 17. Colour and Alpha values of each vertex correspond to the transmittance values used in the environmental simulation. Polygons were grouped and sorted by colour attribute and then sent to Grasshopper for environmental analysis.

TABLE 7 Model variations of mesh density and gradient steps.

	Phase 1 Model (P1)	Low Poly Model (LP)	Medium Poly Model (MP)	High Poly Model (HP)
Number of polygons	10396	192	768	3072
Number of gradient steps	202	9	9	9
	-	18	18	18
	-	36	36	36
	-	-	-	180

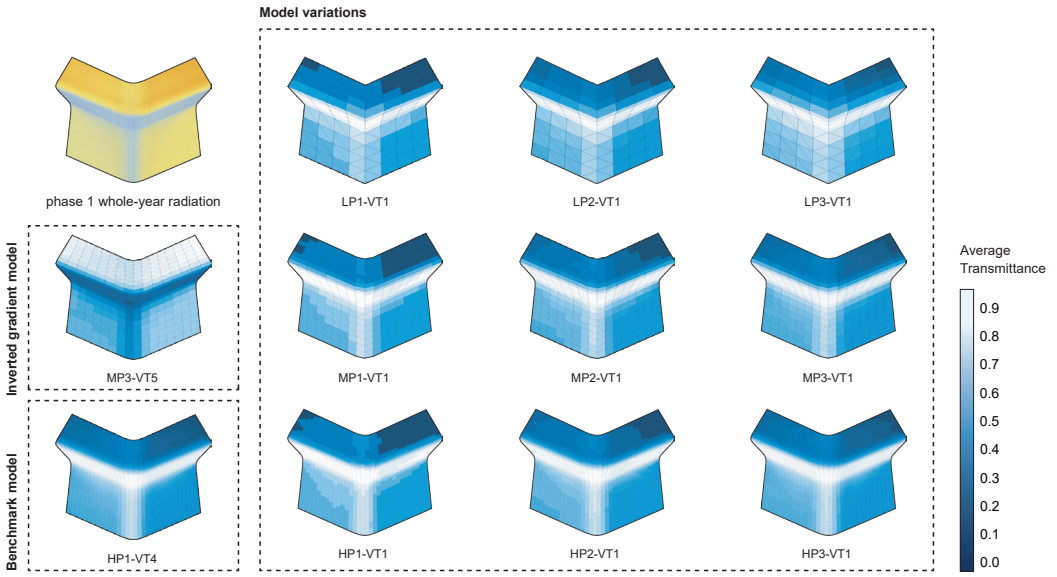

FIG. 17 Phase 1: Optimal façade geometry with whole-year solar radiation heatmap, and Phase 2: Optimised transmittance model variations.

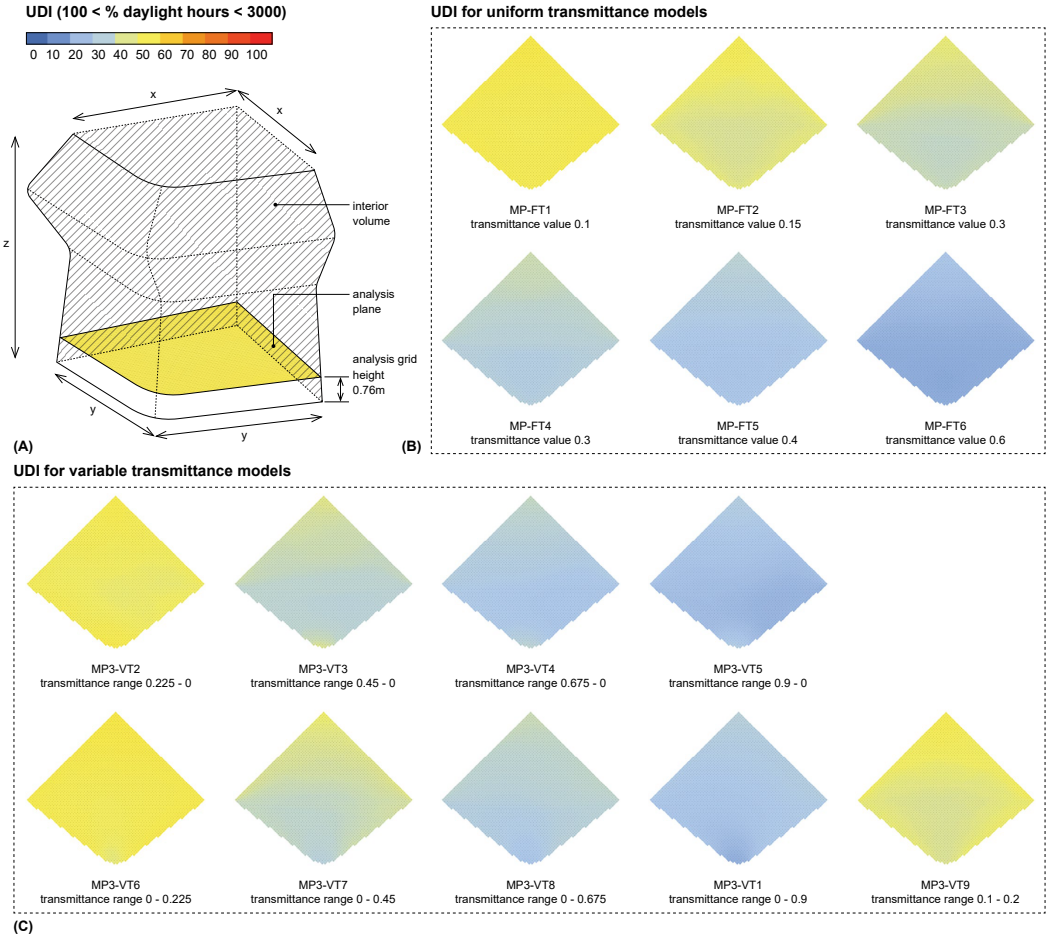

FIG. 18 Diagram of (a) the interior volume, working plane height, and open plan layout alongside UDI analysis heatmaps of (b) uniform and (c) variable transmittance models.

3.2.2 Daylight Performance Analysis

The output mesh groups were mapped to HB transmittance values based on their sorting, within a range of 0 to 0.9, and used to construct an HB model from faces. This simulation uses the London Heathrow weather file as its climatic input. DA was evaluated against a 500-lux threshold, representing a high-performing minimum target illuminance specified in (BS EN 17037:2018, 2021). UDI was assessed within the 100-3000 lux range, capturing a broad spectrum of daylight conditions suitable for office environments. An occupancy programme representing a typical large office was used to define the occupancy schedule, weekdays between 8 AM and 5 PM, specifying the number of occupied hours throughout the year. An open plan floor plan was defined for the occupancy layout. Analysis results were collected for key daylight metrics on a working plane height of 0.76m, including Spatial Daylight Autonomy (sDA), Autonomous Useful Daylight Illuminance (UDI-a), Non-useful Daylight Illuminance (UD-n), and Excessive Daylight Illuminance (UDI-x), each expressed as a percentage of the occupied hours. FIG 18(a) shows the defined interior volume, working plane, and open-plan occupancy layout. UDI-a captures the percentage of occupied hours when illuminance is within the useful range of 100–3000 lux, thereby supporting visual comfort without the need for supplementary lighting. UDI-n captures the percentage of occupied hours when illuminance is below 100 lux, indicating underlit conditions requiring artificial lighting. UDI-x captures the percentage of occupied hours when illuminance exceeds 3000 lux, representing over-lit conditions that may cause glare or visual discomfort (Education Funding Agency, 2014). The aim for each performance metric is shown in TABLE 8.

TABLE 8 Performance criteria aims.

Performance Criteria	Unit	Objective
Autonomous Useful Daylight Illuminance (UDI-a)	%	Max
Non-useful Daylight Illuminance (UD-n)	%	Min
Excessive Daylight Illuminance (UDI-x)	%	Min
Spatial Daylight Autonomy (sDA)	%	Max

TABLE 9 Average DA, UDI-a, UDI-n, UDI-x and simulation run times for different model variations. (Model naming convention: LP: Low polygon count, MP: Medium polygon count, HP: High polygon count, VT: Variable transmittance, FT: Fixed Transmittance)

Model Variations	Faces	Steps	Transmittance Rang	Time (mins)	verage DA 500 (%)	Average UDI-a (%)	Average UDI-n (%)	Average UDI-x (%)
LP1-VT1	192	9	0 - 0.9	4.6	62.28	25.19	32.26	42.55
LP2-VT1	192	18	0 - 0.9	3.6	62.35	24.93	32.23	42.84
LP3-VT1	192	36	0 - 0.9	3.9	63.14	22.35	32.01	45.64
MP1-VT1	768	9	0 - 0.9	5.8	62.32	25.05	32.24	42.70
MP2-VT1	768	18	0 - 0.9	5.4	62.34	24.97	32.24	42.79
MP3-VT1	768	36	0 - 0.9	5.8	62.32	25.07	32.24	42.69
HP1-VT1	3072	9	0 - 0.9	7.1	62.29	25.17	32.26	42.58
HP2-VT1	3072	18	0 - 0.9	6.1	62.31	25.08	32.25	42.68
HP3-VT1	3072	36	0 - 0.9	8.0	62.32	25.08	32.24	42.68
HP4-VT1	3072	180	0 - 0.9	8.9	62.31	25.11	32.24	42.64

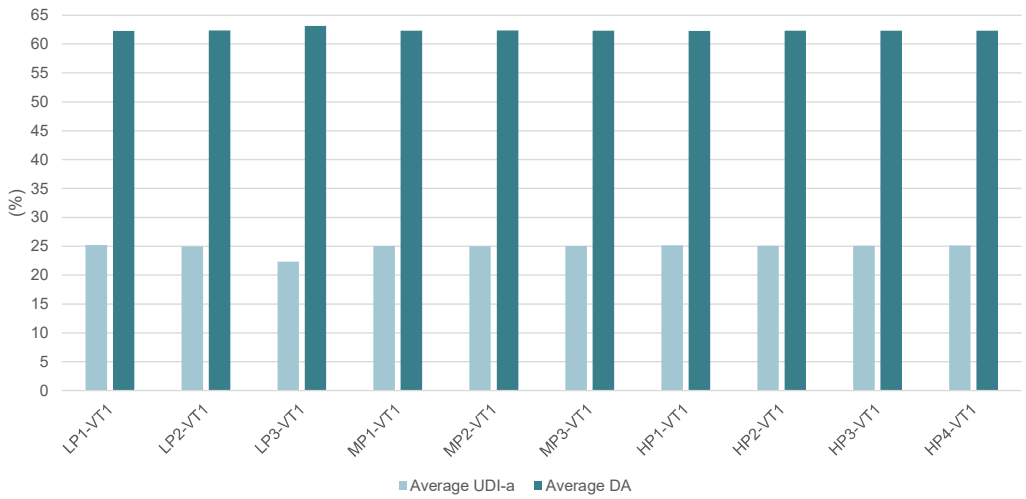

FIG. 19 Bar chart of average UDI-a and DA for the benchmark model and model variations of gradient resolutions.

Evaluating the Impact of Model Resolution on Daylight Analysis Accuracy

Model variations shown in TABLE 9 were first analysed to compare run time and accuracy. The results are compared in FIG 19. In this study, the model variation HP4-VT1 (3072 faces, 180 steps) is used as the benchmark to evaluate the impact of gradient resolution on daylight analysis accuracy across all model iterations, as it has the highest number of steps and mesh resolution, providing the most accurate and closest approximation to a smooth gradient.

To compare the model variations with the benchmark, an Absolute Relative Difference (ARD) was calculated for the mean values of each UDI-a and DA. This is defined as:

$$\mathrm{ARD} = \left| \frac{\bar{\mathbf{x}}_{\text{model variation}} - \bar{\mathbf{x}}_{\text{benchmark}}}{\bar{\mathbf{x}}_{\text{benchmark}}} \right| \times 100$$

The ARD measures the difference between the benchmark mean and each model variation's mean, expressing the magnitude of this difference as a percentage value, as shown in TABLE 10. UDI ARD for LP models differed by an average of 4.02%, MP models by an average of 0.32%, and HP models by an average of 0.17%.

Across all lower-resolution iterations, the DA values remained closely aligned with the benchmark, with a maximum DA ARD of just 1.33%, indicating that gradient and mesh resolution had a minimal impact on the sDA. UDI was more responsive to resolution, with the highest ARD of 11% in model variation *LP3-VT1*, reflecting reduced accuracy in daylight distribution at coarse resolutions. As the resolution increases, particularly in models *MP3-VT1* and *HP3-VT1*, UDI converges toward the benchmark, with differences of less than 0.2%, indicating near-equivalent accuracy.

TABLE 10 The DA ARD and UDI-a ARD for each model variation.

Model Variations	Faces	Steps	DA ARD (%)	UDI-a ARD (%)
LP1-VT1	192	9	0.05	0.32
LP2-VT1	192	18	0.07	0.73
LP3-VT1	192	36	1.33	11.02
MP1-VT1	768	9	0.02	0.24
MP2-VT1	768	18	0.05	0.55
MP3-VT1	768	36	0.02	0.18
HP1-VT1	3072	9	0.03	0.22
HP2-VT1	3072	18	0.00	0.14
HP3-VT1	3072	36	0.01	0.15

This trend indicates that while increased gradient resolution has minimal influence on sDA, it does affect UDI accuracy. The results also demonstrate that simulation time is predominantly influenced by model complexity, with computation time increasing with the number of faces, as shown in FIG 20. In contrast, the number of transmittance steps exhibits a less predictable impact on simulation time. Based on the results, an MP model complexity of 768 faces was selected to determine the optimal transmittance range.

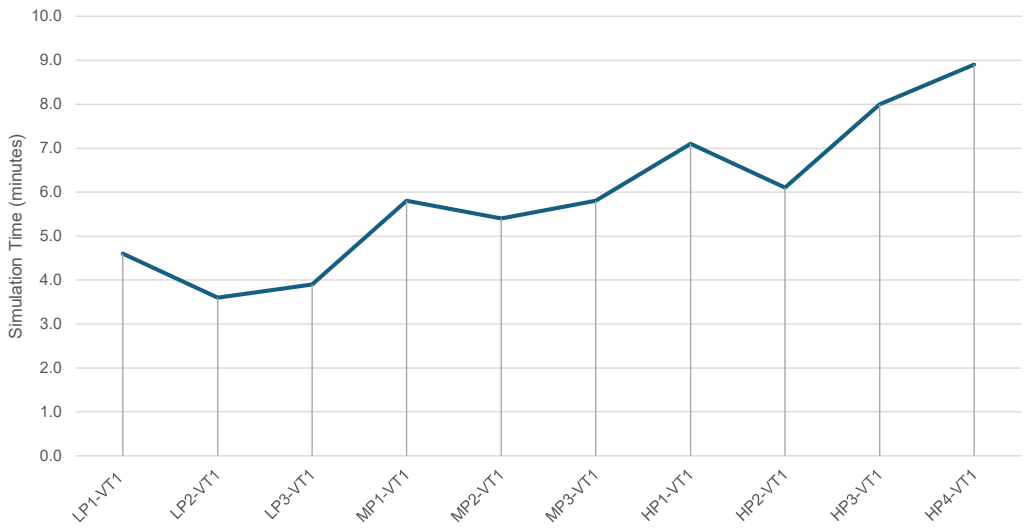

FIG. 20 Line chart of simulation runtimes across model variations.

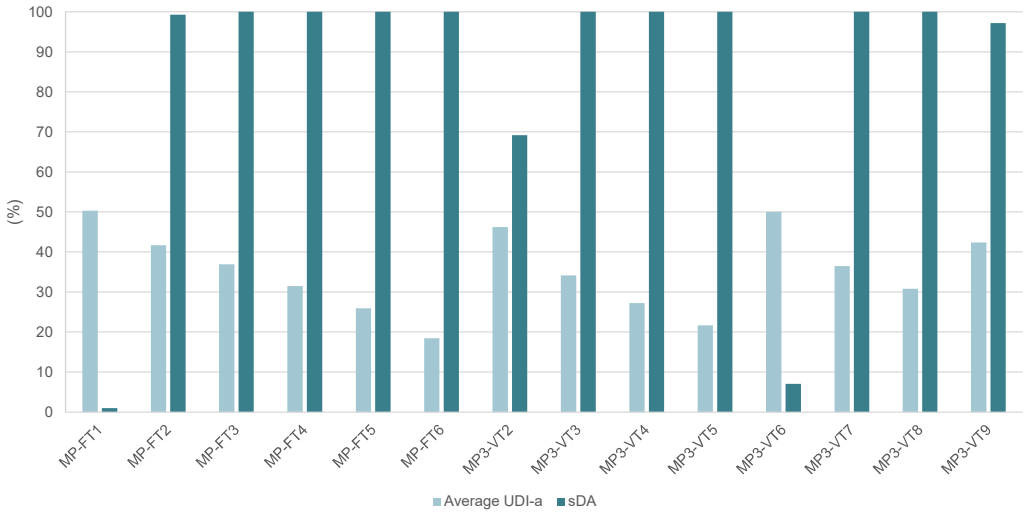

FIG. 21 Bar chart of average UDI-a and sDA for uniform and variable transmittance models.

Determining the Optimal Transmittance Range for Daylight Performance

Additional model variations, shown in TABLE 11 and FIG 21, were analysed to determine the optimal transmittance range for the gradient design.

Based on the Department for Education (DfE) daylight performance criteria (Department for Education, 2022), a scoring methodology was developed to quantitatively compare and rank the performance of each model variation. Models achieving an sDA of 50% or greater were assigned a maximum score of 1. Models below this threshold were scored proportionally, scaled between 0 and 1, defined as:

$$\mathrm{sDA}_{\mathrm{score}} = \frac{\mathrm{sDA}}{50}$$

For UDI-a, with a target of 80% within the 100-3000 lux range, the score was based on the absolute difference from this target, normalised between 0 and 1, defined as:

$$\mathrm{UDI}_{\mathrm{score}} = 1 - \frac{|\mathrm{UDI} - 80|}{80}$$

A composite score was then calculated, providing a single performance indicator that integrates both daylight sufficiency and distribution quality, as presented in TABLE 12. This was defined as:

$$\text{Composite Score} = \frac{\mathrm{sDA}_{\mathrm{score}} + \mathrm{UDI}_{\mathrm{score}}}{2}$$

Among the uniform transmittance models, *MP-FT1* (0.1 fixed transmittance) demonstrated the best UDI-a performance with an average of 50.32%; however, the sDA achieved 0%, resulting in the lowest composite score (0.31). *MP-FT2* (0.15 fixed transmittance) achieved the highest composite score (0.76) with an sDA of 99.27% and an average UDI-a of 41.69%.

As transmittance increased, UDI-a declined significantly, indicating a higher risk of daylight discomfort due to excessive illuminance as reflected in higher UDI-x values.

TABLE 11 Simulation run times, average DA, sDA, average UDI, average UDI-n, and average UDI-x for fixed and variable transmittance models.

Model Variations	Faces	Steps	Transmittance Range	Average DA 500 (%)	SDA 500,50% (%)	Average UDI-a (%)	Average UDI-n (%)	Average UDI-x (%)
MP-FT1	768	-	0.1	46.54	0	50.32	37.53	12.15
MP-FT2	768	-	0.15	52.93	99.27	41.69	35.22	23.10
MP-FT3	768	-	0.2	56.83	100	36.93	34.00	29.07
MP-FT4	768	-	0.3	60.40	100	31.48	32.76	35.76
MP-FT5	768	-	0.4	62.16	100	25.93	32.26	41.82
MP-FT6	768	-	0.6	64.53	100	18.50	31.65	49.85
MP3-VT2	768	36	0.225 – 0	50.44	69.21	46.24	36.08	17.68
MP3-VT3	768	36	0.45 – 0	59.11	100	34.16	33.16	32.68
MP3-VT4	768	36	0.675 – 0	61.87	100	27.27	32.35	40.37
MP3-VT5	768	36	0.9 – 0	63.52	100	21.72	31.88	46.41
MP3-VT6	768	36	0 – 0.225	46.51	7.09	50.04	37.57	12.40
MP3-VT7	768	36	0 – 0.45	56.90	100	36.50	34.00	29.50
MP3-VT8	768	36	0 – 0.675	60.44	100	30.83	32.75	36.41
MP3-VT9	768	36	0.1 – 0.2	52.39	97.18	42.38	35.43	22.19

TABLE 12 *Composite score analysis indicated that the sDA score, UDI-a score, and combined score ranked from best to worst performance.*

Optimised Model	sDA Score	UDI Score	Composite Score
MP3-VT2	1	0.58	0.79
MP3-VT9	1	0.53	0.76
MP-FT2	1	0.52	0.76
MP-FT3	1	0.46	0.73
MP3-VT7	1	0.46	0.73
MP3-VT3	1	0.43	0.71
MP-FT4	1	0.39	0.70
MP3-VT8	1	0.39	0.69
MP3-VT4	1	0.34	0.67
MP-FT5	1	0.32	0.66
MP3-VT5	1	0.27	0.64
MP-FT6	1	0.23	0.62
MP3-VT6	0.14	0.63	0.38
MP-FT1	0	0.63	0.31

The variable transmittance model *MP3-VT2* achieved the highest composite score (0.79) among all fixed and variable models, demonstrating a balanced performance across daylight sufficiency (average DA = 50.44%), distribution (sDA = 69.21%), and daylight quality (average UDI-a = 46.24%). Among the variable transmittance models, *MP3-VT6* achieved the highest UDI-a (50.04%); however, again at the cost of sDA (7.09%).

TABLE 13 Results for average DA, sDA, average UDI, average UDI-n, average UDI-x, and Composite Score of a fully glazed curtain wall model, compared with the fixed transmittance model MP-FT6 and the best performing model MP3-VT2.

	Transmittance Range	Average DA 500 (%)	sDA 500,50% (%)	Average UDI-a (%)	Average UDI-n (%)	Average UDI-x (%)	Composite Score
Curtain Wall Model	0.6	63.82	100	20.30	31.80	47.91	0.63
MP-FT6	0.6	64.53	100	18.50	31.65	49.85	0.62
MP3-VT2	0.225 – 0	50.44	69.21	46.24	36.08	17.68	0.79

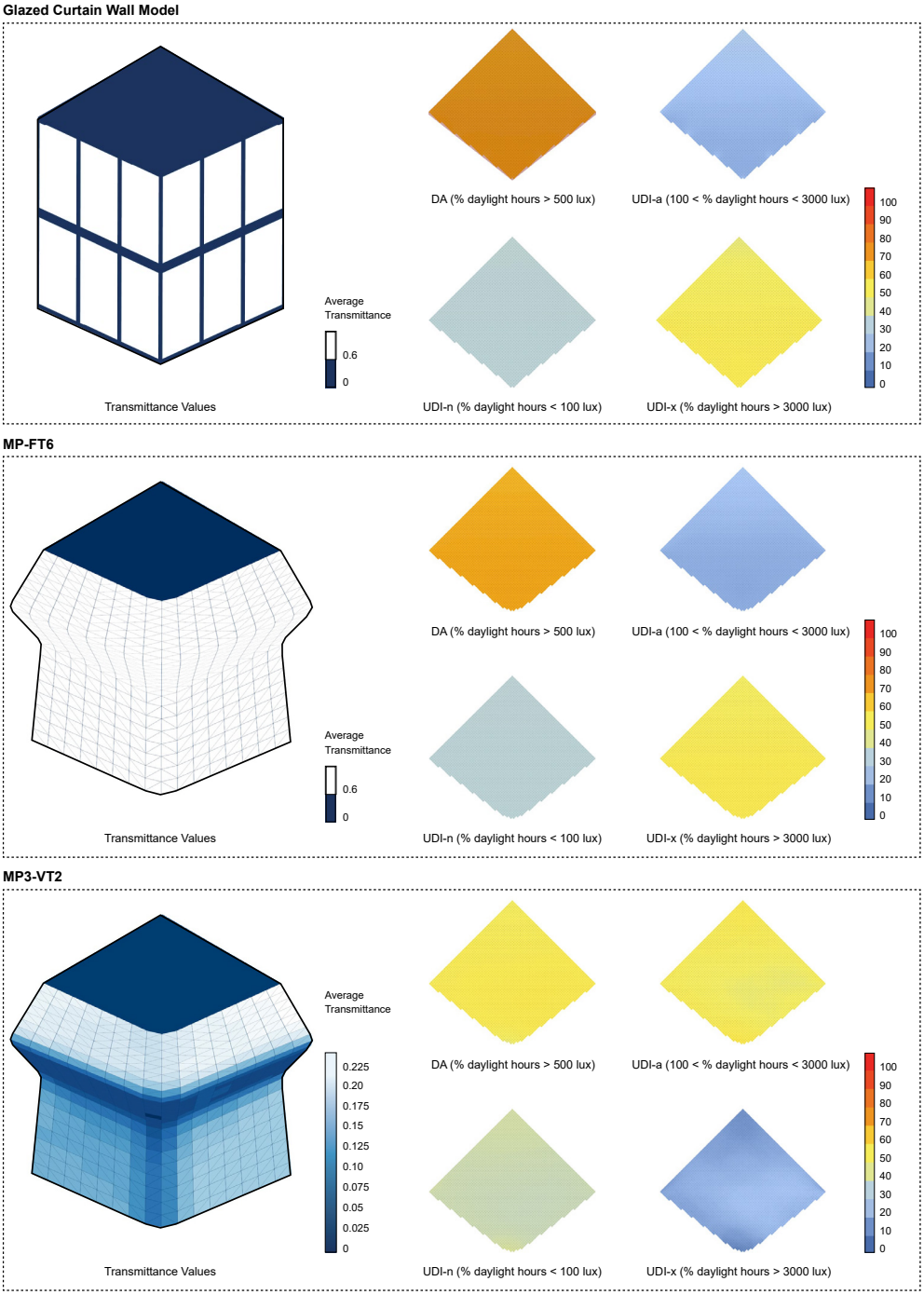

FIG. 22 Diagram of transmittance values and associated DA, UDI, UDI-n, and UDI-x for the Glazed Curtain Wall Model, MP-FT6 and MP3-VT2.

Comparative Analysis

To conclude Phase 2, an analysis of a fully glazed curtain wall façade, with a window-to-wall ratio of 92% on the south-facing walls, in the same position and orientation, was conducted as a further comparison against a fixed transmittance model, *MP-FT6*, and the best-performing variable transmittance model, *MP3-VT2*, shown in TABLE 13 and FIG 22.

MP-FT6 represents the optimal geometry identified in Section 3.1, without any subsequent optimisation of transmittance gradients. In this configuration, a uniform transmittance value of 0.6 is applied, matching that of the glazed curtain wall. As expected, when no transmittance gradients are introduced, the performance of the optimal geometry resembles that of the fully glazed reference façade. The results demonstrate that the variable transmittance model MP3-VT2, which combines optimal geometry with optimised transmittance gradients (shown in FIG 23), significantly outperforms a conventional fully glazed curtain wall system, improving the UDI-a by 25.94%, from 20.30% to 46.24%. Although most model variations exceeded the sDA targets for this study, none achieved a UDI-a target of 80% within the 100-3000 lux range.

Numerous factors may contribute to the target of 80% UDI-a not being achieved. Firstly, the entire room is likely to be underlit during specific periods of the year, particularly in winter mornings and late afternoons when exterior illuminance is naturally low. This is evident from the fully glazed curtain wall, which still yields a UDI-n of 31.80%, indicating that even with maximum daylight exposure for this orientation and configuration, a significant percentage of occupied hours remain underlit. This also suggests that an 80% UDI-a is a highly ambitious year-round target for the occupancy schedule used in this study. Another factor to consider is the specific gradient transmittance pattern applied. In this study, the patterns closely follow the initial solar radiation heatmap on the façade surface. Although the transmittance ranges were adjusted and inverted, the underlying distribution pattern remained essentially unchanged, which is a limitation of the gradient optimisation method. Alternative gradient configurations may therefore yield UDI-a values that exceed those achieved in the current set of models.

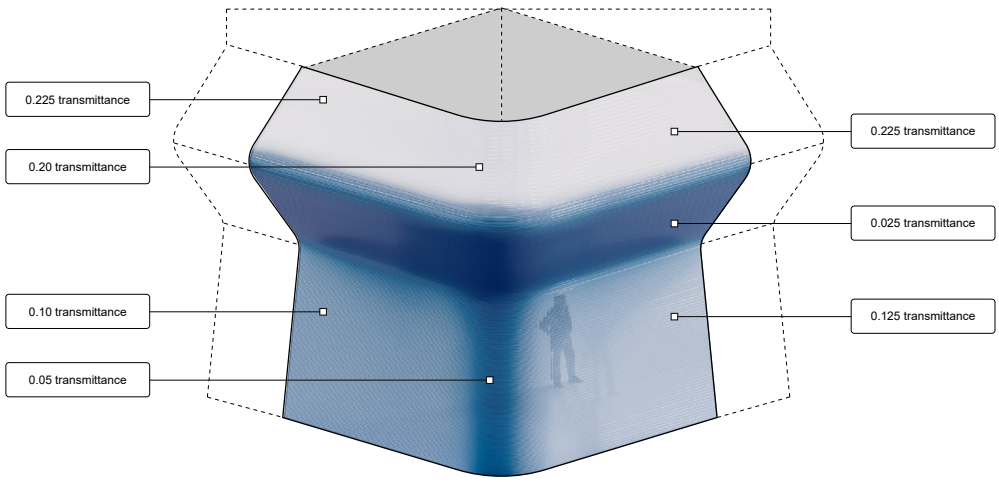

FIG. 23 Diagram of the best-performing variable transmittance model MP3-VT2 demonstrating the gradient applied to the optimal geometry.

4 CONCLUSION

This study investigated the digital design of PETG façades with variable transmittance properties intended for future fabrication via LSR3DP, addressing two fundamental questions: how can multiobjective optimisation be applied to identify façade forms that balance solar performance with structural efficiency, and how can solar-informed transmittance gradients be systematically distributed and discretised to achieve comfortable daylight levels?

The study demonstrates that multiobjective optimisation using NSGA-II can effectively navigate complex design trade-offs, identifying geometrically optimised façades that significantly outperform conventional vertical configurations, achieving reductions in summer solar radiation of up to 13.99% and increases in winter solar gain of up to 26.8% for different orientations whilst maintaining acceptable structural displacement. More significantly, the systematic application of solar-informed transmittance gradients through procedural discretisation workflows proved highly effective for daylight control, with the optimal configuration delivering a 25.94% improvement in Useful Daylight Illuminance compared to a standard curtain wall system. This performance gain was achieved through material-based light modulation rather than mechanical shading devices, validating the premise that transmittance variations can be embedded directly into the façade system to provide spatially responsive daylight control. The results establish that unified, multi-property envelopes enabled by LSR3DP can compete with, and in key metrics exceed, the performance of conventional multilayered façade assemblies.

4.1 SUMMARY OF KEY RESULTS

The proposed two-phase methodology established a unified workflow that responds to both structural and environmental performance criteria.

In Phase 1, a script was developed to generate a diverse range of corner façade geometries, defined by eight geometric parameters. Sensitivity analysis revealed strong correlations between specific parameters and the three target performance objectives, providing insight into which aspects of the geometry most influence environmental and structural outcomes. A multiobjective optimisation process, implemented using the NSGA-II algorithm, was then employed to navigate the extensive design space and identify façade solutions that balanced competing objectives. Sixteen optimal configurations were identified across four main orientations, including solutions individually optimised for solar exposure and structural deformation, as well as aggregated solutions ranked via TOPSIS.

When focusing on the south-oriented façade, additional insights emerged regarding how displacement interacted with the environmental objectives and influenced the resulting geometries. The optimal solution for summer solar reduction exhibited a pronounced overhang, effectively casting self-shade over the lower portions of the façade to reduce incident radiation. This shading strategy resulted in the most geometrically articulated form, with the largest surface area and the highest structural displacement among the four solutions, highlighting a clear trade-off between environmental control and structural stability. In contrast, the displacement-optimal solution, the winter solar-optimal solution, and the TOPSIS-optimal solution shared a similar, more linear profile. These configurations exhibited minimal surface articulation and a more compact geometry, leading to reduced displacement and smaller surface areas. While the winter solar solution introduced a subtle surface extension to enhance solar gain during low-angle winter sun conditions, its

overall form remained closely aligned with the structurally efficient displacement-optimal variant. The resemblance among these three solutions suggests a convergence in which structural stability and seasonal solar access can be achieved without excessive formal complexity.

Building on the south-oriented optimal geometry, Phase 2 focused on exploring daylight performance by applying solar-informed transmittance gradients. A procedural workflow was developed to discretise and apply gradient values across the façade surface, replacing the conventional aperture-based daylighting approach. Rather than relying on windows embedded within an opaque envelope, this method modulates light transmission continuously through localised variations in material transparency, offering a more nuanced and spatially resolved form of daylight control.

Simulations conducted in Phase 2 using multiple mesh densities and gradient resolutions confirmed that while spatial daylight autonomy (sDA) remained relatively stable across all model variations, useful daylight illuminance (UDI-a) was more sensitive to resolution and benefited significantly from finer gradient control. A detailed comparative analysis revealed that lower-resolution meshes, particularly those with fewer polygons, led to notable deviations in UDI-a accuracy. In contrast, higher-resolution models provided greater precision but at the cost of significantly longer simulation times. Interestingly, the number of gradient steps had minimal effect on sDA and a less predictable impact on runtime, whereas mesh complexity was the dominant factor influencing computational demand.

Based on the trade-off between accuracy and simulation efficiency, the medium-resolution model with 768 polygons was selected for the final transmittance range analysis. This configuration offered near-equivalent performance to the high-resolution benchmark while substantially reducing computation time, making it the most practical choice for the remaining daylight simulations. The highest-performing variable transmittance model demonstrated substantial improvements in daylight distribution and quality compared to both uniform transmittance alternatives and a fully glazed curtain wall benchmark. These improvements were achieved without sacrificing structural integrity or geometric expressiveness. The findings demonstrate that by embedding environmental data directly into the form and material logic of the façade, it is possible to produce adaptive, performance-optimised surfaces that integrate structural and daylighting functions holistically.

4.2 STUDY IMPLICATIONS

This integrated approach presents a significant shift from conventional façade strategies, offering new opportunities for environmentally responsive architecture through the interaction of digital fabrication, parametric modelling, and environmental simulation.

The scientific relevance of these findings extends beyond the specific geometry and transmittance values identified. This work establishes quantitative benchmarks for evaluating unified, multi-property building envelopes: the improvement in daylight quality demonstrates that material-based transmittance modulation can achieve performance levels previously requiring mechanical shading systems, whilst the geometric analysis reveals that moderate formal complexity can deliver comparable environmental benefits to highly articulated forms, while maintaining structural efficiency. These outcomes challenge conventional assumptions that high-performing façades necessitate either complex geometries or mechanical systems.

By demonstrating measurable improvements across multiple performance criteria through embedded material properties, this study provides empirical evidence supporting the technical feasibility of LSR3DP-enabled façades as viable alternatives to conventional multilayered assemblies. The discretisation methodology developed in Phase 2 addresses a critical gap in translating continuous performance data into stepped transmittance zones suitable for simulation and eventual fabrication, establishing practical guidance for balancing computational accuracy against simulation efficiency in performance-driven façade design.

4.3 LIMITATIONS AND FUTURE WORK

The simulated transmittance values used in this study relied on proxy material properties and uniform optical behaviour, which can differ significantly from the actual performance of 3D-printed structures. In practice, factors such as print resolution, layer thickness, surface roughness, and internal infill geometry introduce variability in light transmission that daylight simulations often fail to capture. The anisotropic nature of printed layers, combined with material-specific scattering and absorption effects, can substantially alter both the quantity and quality of transmitted light. As a result, empirical testing would be essential to validate and calibrate simulation data, ensuring that predicted daylight performance more closely aligns with physical behaviour. Future research should prioritise physical prototyping and empirical validation of the transmittance gradients, alongside the exploration of fabrication strategies to realise multi-property PETG façades at an architectural scale.

References

BS EN 17037:2018. (2021). BSI. https://knowledge.bsigroup.com/products/daylight-in-buildings-1

Bollinger, K., Grohmann, M., & Tessman, O. (2010). Form follows performance. In *Symposium on Simulation for Architecture and Urban Design*.

Castañeda, E., Lauret, B., Lirola, J. M., & Ovando, G. (2015). Free-form architectural envelopes: Digital processes opportunities of industrial production at a reasonable price. *Journal of Façade Design and Engineering*, *3*(1), 1–13. https://doi.org/10.3233/fde-150031

Cheibas, I., Gamote, R. P., Lloret-Fritschi, E., Arnold, K., Luible, A., Gramazio, F., & Kohler, M. (2024). 3D printing of a multi-performative building envelope: Assessment of air permeability, water tightness, wind loads, and impact resistance. *Journal of Building Engineering*, *98*. https://doi.org/10.1016/j.jobe.2024.111251

Cheibas, I., Piccioni, V., Lloret-Fritschi, E., Leschok, M., Schlüter, A., Dilllenburger, B., Gramazio, F., & Kohler, M. (2023). Light Distribution in 3D-Printed Thermoplastics. *3D Printing and Additive Manufacturing*, *10*(6), 1164–1177. https://doi.org/10.1089/3dp.2023.0050

Department for Education. (2022). *School Output Specification Technical Annex 2E: Daylight and Electric Lighting*. https://assets.publishing.service.gov.uk/media/637e13508fa8f56eb1a0ad14/GDB_Annex_2E_DaylightAndElectricLighting-A-C11.pdf

Education Funding Agency. (2014). *Baseline Design-Daylight Strategy*. https://assets.publishing.service.gov.uk/media/5b3b6a27ed915d33ced545ca/Baseline_designs_daylight_strategy_Dec_2014.pdf

Engelsmann, S., Spalding, V., & Peters, S. (2010). *Plastics*. https://doi.org/10.1515/9783034611947

Fan, Z., Liu, M., & Tang, S. (2022). A multiobjective optimization design method for gymnasium façade shading ratio integrating energy load and daylight comfort. *Building and Environment*, *207*. https://doi.org/10.1016/j.buildenv.2021.108527

Grigoriadis, K., & Lee, G. (2024). *3D printing and material extrusion in architecture: Construction and design manuals*. DOM Publishers.

Grigoriadis, K. (2018). The current state of autography. *International Journal of Rapid Manufacturing, 7* (2/3), 277–294. https://doi.org/10.1504/IJRAPIDM.2018.092902

Grigoriadis, K. (2019). Computational blends: The epistemology of designing with functionally graded materials. *Journal of Architecture*, *24*(2), 160–192. https://doi.org/10.1080/13602365.2019.1578074

Hwang, CL., Yoon, K. (1981). Methods for Multiple Attribute Decision Making. In: Multiple Attribute Decision Making. Lecture Notes in Economics and Mathematical Systems, vol 186. Springer, Berlin, Heidelberg. https://doi.org/10.1007/978-3-642-48318-9_3

K. Deb, A. Pratap, S. Agarwal and T. Meyarivan, "A fast and elitist multiobjective genetic algorithm: NSGA-II," in IEEE Transactions on Evolutionary Computation, vol. 6, no. 2, pp. 182-197, April 2002, doi: 10.1109/4235.996017.

Kwon, H., Kyttas, T., Eichenhofer, M., & Dillenburger, B. (2019). Digital Composites: Robotic 3D Printing of Continuous Carbon Fiber-Reinforced Plastics for Functionally-Graded Building Components. *Robotic Fabrication in Architecture, Art and Design 2018: Foreword by Sigrid Brell-Çokcan and Johannes Braumann, Association for Robots in Architecture*, 363–376. https://doi.org/10.1007/978-3-319-92294-2_28

Lin, C. H., & Tsay, Y. S. (2024). A practical decision process for building façade performance optimization by integrating machine learning and evolutionary algorithms. *Journal of Asian Architecture and Building Engineering*, *23*(2), 740–753. https://doi.org/10.1080/13467581.2023.2244564

Milano, F., Gamote, R. P., Olivo, N. E., Piccioni, V., Chen, P. Y., Gallagher, C., Schlueter, A., Dillenburger, B., Luible, A., Gramazio, F., & Kohler, M. (2024). Integration of a 3D-Printed Façade Unit in a Curtain Wall System: Prototyping and Assessment. *Journal of Façade Design and Engineering*, *12*(1), 9–28. https://doi.org/10.47982/jfde.2024.325

Mungenast, M. (2017). 3d-Printed Low-tech Future Façades – Development of 3d-printed Functional-Geometries for Building Envelopes. *PowerSkin Conference Proceedings* , 307–317.

Piccioni, V., Turrin, M., & Tenpierik, M. J. (2020). A Performance-Driven Approach for the Design of Cellular Geometries with Low Thermal Conductivity for Application in 3D-Printed Façade Components. *Of the Symposium on Simulation for Architecture and Urban Design SimAUD*.

Preisinger, C. (2013). Linking structure and parametric geometry. *Architectural Design*, *83*(2), 110-113. https://doi.org/10.1002/ad.1564

Robert McNeel & Associates. (n.d.). *Rhinoceros 3D* [Computer software]. Retrieved November 21, 2025, from https://www.rhino3d.com/

Roudsari, M., & Ladybug Tools LLC. (n.d.). *Ladybug Tools* [Software & documentation]. Retrieved November 21, 2025, from https://www.ladybug.tools/

Rutten, D., & Robert McNeel & Associates. (n.d.). *Grasshopper 3D* [Visual programming environment]. Retrieved November 21, 2025, from https://www.grasshopper3d.com/

Quillet, A., & Rogan, D. (2022). *Wonova: the future of façades? - Eckersley O'Callaghan*. https://www.eocengineers.com/wonova-the-future-of-facades/

Sarakinioti, M. V., Turrin, M., Konstantinou, T., Tenpierik, M., & Knaack, U. (2018). Developing an integrated 3D-printed façade with complex geometries for active temperature control. *Materials Today Communications*, *15*, 275–279. https://doi.org/10.1016/j.mtcomm.2018.02.027

Shan, R., & Shi, T. (2016). Multiobjective optimization of building façade design strategies. In *Proceedings of the 3rd Asia Conference of the International Building Performance Simulation Association (ASim 2016)*. IBPSA.

Showkatbakhsh, M., Makki, M., & Song, Y. (n.d.). *Wallacei* [Software plugin]. Retrieved August 1, 2025, from https://www.wallacei.com/

SideFX. (n.d.). (n.d.). *Attribute Transfer*. Retrieved July 27, 2025, from https://www.sidefx.com/docs/houdini/nodes/sop/attribtransfer.html

Taseva, Y., Eftekhar, N., Kwon, H., Leschok, M., & Dillenburger, B. (2020). *LARGE-SCALE 3D PRINTING FOR FUNCTIONALLY-GRADED FAÇADE* (Vol. 1).

Tee, Y. L., Peng, C., Pille, P., Leary, M., & Tran, P. (2020). PolyJet 3D Printing of Composite Materials: Experimental and Modelling Approach. *JOM*, *72*(3), 1105–1117. https://doi.org/10.1007/s11837-020-04014-w

Tenpierik, M., Turrin, M., Wattez, Y., Cosmatu, T., & Tsafou, S. (2018). *View of Double Face 2.0: A lightweight translucent adaptable Trombe wall | SPOOL*. https://spool.ac/index.php/spool/article/view/86/85

Vazquez, E., & Duarte, J. (2022). Exploring the Impact of Geometry and Fibre Arrangements on Daylight Control in Bistable Kinetic Shades. *Journal of Façade Design and Engineering*, *10*(1). https://doi.org/10.47982/jfde.2022.1.03

Wagiri, F., Shih, S. G., Harsono, K., & Wijaya, D. C. (2024). Multiobjective optimization of kinetic façade aperture ratios for daylight and solar radiation control. *Journal of Building Physics*, *47*(4), 355–385. https://doi.org/10.1177/17442591231219793

Yuan, P. F., Beh, H. S., Yang, X., Zhang, L., & Gao, T. (2022). Feasibility study of large-scale mass customization 3D printing framework system with a case study on Nanjing Happy Valley East Gate. *Frontiers of Architectural Research*, *11*(4), 670–680. https://doi.org/10.1016/j.foar.2022.05.005